The Astronomical Journal, 154:159 (23pp), 2017 October https://doi.org/10.3847/1538-3881/aa8956
© 2017. The American Astronomical Society. All rights reserved.

Size and Shape of Chariklo from Multi-epoch Stellar Occultations*

R. Leiva[1,2], B. Sicardy[1], J. I. B. Camargo[3,4], J.-L. Ortiz[5], J. Desmars[1], D. Bérard[1], E. Lellouch[6], E. Meza[1], P. Kervella[1,7], C. Snodgrass[8], R. Duffard[5], N. Morales[5], A. R. Gomes-Júnior[9], G. Benedetti-Rossi[3,4], R. Vieira-Martins[3,4,9], F. Braga-Ribas[3,4,10], M. Assafin[9], B. E. Morgado[3], F. Colas[11], C. De Witt[12], A. A. Sickafoose[13,14], H. Breytenbach[13,15], J.-L. Dauvergne[16], P. Schoenau[12], L. Maquet[11], K.-L. Bath[12,17], H.-J. Bode[12,17,25], A. Cool[18,19], B. Lade[18,19,20], S. Kerr[21,22], and D. Herald[21,23,24]

[1] LESIA/Observatoire de Paris, CNRS UMR 8109, Université Pierre et Marie Curie, Université Paris-Diderot, 5 place Jules Janssen, F-92195 Meudon Cédex, France; rnleiva@uc.cl
[2] Instituto de Astrofísica, Facultad de Física, Pontificia Universidad Católica de Chile, Av. Vicuña Mackenna 4860, Santiago, Chile
[3] Observatório Nacional/MCTIC, Rua General José Cristino 77, RJ 20921-400, Rio de Janeiro, Brazil
[4] Laboratório Interinstitucional de e-Astronomia—LIneA, Rua General José Cristino 77, RJ 20921-400, Rio de Janeiro, Brazil
[5] Instituto de Astrofísica de Andalucía, CSIC, Glorieta de la Astronomía s/n, E-18008, Granada, Spain
[6] LESIA, Observatoire de Paris, PSL Research University, CNRS, Sorbonne Universités, UPMC Univ. Paris 06, Univ. Paris Diderot, Sorbonne Paris Cité, 5 place Jules Janssen, F-92195 Meudon, France
[7] Unidad Mixta Internacional Franco-Chilena de Astronomía (CNRS UMI 3386), Departamento de Astronomía, Universidad de Chile, Camino El Observatorio 1515, Las Condes, Santiago, Chile
[8] School of Physical Sciences, The Open University, Milton Keynes, MK7 6AA, UK
[9] Observatório do Valongo/UFRJ, Ladeira Pedro Antonio 43, RJ 20.080-090, Rio de Janeiro, Brazil
[10] Federal University of Technology- Paraná (UTFPR/DAFIS), Rua Sete de Setembro, 3165, CEP 80230-901, Curitiba, PR, Brazil
[11] IMCCE, Observatoire de Paris, PSL Research University, CNRS, Sorbonne Universités, UPMC Univ. Paris 06, 77 Av. Denfert-Rochereau, F-75014, Paris, France
[12] IOTA/ES, Barthold-Knaust-Strasse 8, D-30459 Hannover, Germany
[13] South African Astronomical Observatory, P.O. Box 9, 7935 Observatory, South Africa
[14] Department of Earth, Atmospheric, and Planetary Sciences, Massachusetts Institute of Technology, Cambridge, MA 02139-4307, USA
[15] Department of Astronomy, University of Cape Town, Rondebosch, Cape Town, 7700, South Africa
[16] AFA/Ciel et Espace, 17 Emile Deutsch de la Meurthe, F-75014, Paris, France
[17] Internationale Amateursternwarte e. V. IAS, Hakos/Namibia and Bichler Str. 46, D-81479, Munich, Germany
[18] Defence Science & Technology Group, P.O. Box 1500, Edinburgh SA 5111, Australia
[19] The Heights Observatory, 12 Augustus St, Modbury Heights SA 5092, Australia
[20] Stockport Observatory, Astronomical Society of South Australia, Stockport, SA, Australia
[21] Occultation Section of the Royal Astronomical Society of New Zealand (RASNZ), P.O. Box 3181, Wellington, New Zealand
[22] Astronomical Association of Queensland, 5 Curtis Street, Pimpama QLD 4209, Australia
[23] International Occultation Timing Association (IOTA), P.O. Box 7152, Kent, WA 98042, USA
[24] Canberra Astronomical Society, Canberra, ACT, Australia
Received 2017 July 7; revised 2017 August 28; accepted 2017 August 28; published 2017 September 22

Abstract

We use data from five stellar occultations observed between 2013 and 2016 to constrain Chariklo's size and shape, and the ring reflectivity. We consider four possible models for Chariklo (sphere, Maclaurin spheroid, triaxial ellipsoid, and Jacobi ellipsoid), and we use a Bayesian approach to estimate the corresponding parameters. The spherical model has a radius $R = 129 \pm 3$ km. The Maclaurin model has equatorial and polar radii $a = b = 143^{+3}_{-6}$ km and $c = 96^{+14}_{-4}$ km, respectively, with density 970^{+300}_{-180} kg m^{-3}. The ellipsoidal model has semiaxes $a = 148^{+6}_{-4}$ km, $b = 132^{+6}_{-5}$ km, and $c = 102^{+10}_{-8}$ km. Finally, the Jacobi model has semiaxes $a = 157 \pm 4$ km, $b = 139 \pm 4$ km, and $c = 86 \pm 1$ km, and density 796^{+2}_{-4} kg m^{-3}. Depending on the model, we obtain topographic features of 6–11 km, typical of Saturn icy satellites with similar size and density. We constrain Chariklo's geometric albedo between 3.1% (sphere) and 4.9% (ellipsoid), while the ring I/F reflectivity is less constrained between 0.6% (Jacobi) and 8.9% (sphere). The ellipsoid model explains both the optical light curve and the long-term photometry variation of the system, giving a plausible value for the geometric albedo of the ring particles of 10%–15%. The derived mass of Chariklo of 6–8 $\times 10^{18}$ kg places the rings close to 3:1 resonance between the ring mean motion and Chariklo's rotation period.

Key words: methods: statistical – minor planets, asteroids: individual (Chariklo) – occultations – planets and satellites: rings

1. Introduction

The Centaur object (10199) Chariklo is the only small object of the solar system known thus far to show the unambiguous presence of a ring system. It was discovered during a ground-based stellar occultation in 2013 (Braga-Ribas et al. 2014), and confirmed by several subsequent observations (Bérard et al. 2017).

Meanwhile, the basic physical characteristics of Chariklo remain fragmentary. Chariklo's radius estimations, taken from thermal measurements, vary from 108 to 151 km, with geometric albedo in the range 4%–8% (Jewitt & Kalas 1998; Altenhoff et al. 2001; Sekiguchi et al. 2012; Bauer et al. 2013;

* Based on observations obtained at the Southern Astrophysical Research (SOAR) telescope, which is a joint project of the Ministério da Ciência, Tecnologia, e Inovação (MCTI) da República Federativa do Brasil, the U.S. National Optical Astronomy Observatory (NOAO), the University of North Carolina at Chapel Hill (UNC), and Michigan State University (MSU).
[25] Deceased, 2017 July 16.

Fornasier et al. 2014). The 2013 stellar occultation had poor coverage of the main body, which still provides a spheroidal shape with equatorial radius $a = 144.9$ km and polar radius $c = 114$ km.

Rotational light curves obtained in the visible between 1997 and 2013 exhibit a variable peak-to-peak amplitude from non-detectable in 1997 and 1999 to amplitudes of 0.11–0.13 in 2006 and 2013, respectively (Davies et al. 1998; Peixinho et al. 2001; Fornasier et al. 2014; Galiazzo et al. 2016). This can be produced by an elongated body, longitudinal albedo variegations, or more probably, a combination of both. The best measurements provide a rotation period of 7.004 ± 0.036 hr (Fornasier et al. 2014). Spectroscopic measurements show the presence of water ice in the system (Guilbert-Lepoutre 2011; Duffard et al. 2014). Finally, no satellites have been detected around Chariklo, preventing any mass estimation.

The size, shape, and density of Chariklo are important parameters to constrain the origins of both the main body and its rings. Moreover, topographic features and/or an ellipsoidal shape may have a drastic influence in the ring dynamics through resonances between ring mean motion and body rotation.

Here, we use several stellar occultations to put constraints on the size and shape of Chariklo's main body. This technique has been used on several trans-Neptunian objects (TNOs) and Centaur objects, including 2002 TX_{300} (Elliot et al. 2010), Eris (Sicardy et al. 2011), Makemake (Ortiz et al. 2012), Varuna (Sicardy et al. 2010), Quaoar (Braga-Ribas et al. 2013), 2002 KX_{14} (Alvarez-Candal et al. 2014), 2007 UK_{126} (Benedetti-Rossi et al. 2016; Schindler et al. 2017), and 2003 AZ_{84} (Dias-Oliveira et al. 2017).

Due to the very small angular size of Chariklo (~80 milliarcseconds, rings included), predictions of stellar occultations are difficult and coverage of the shadow path is poor, with only a few chords on the body per event. In order to retrieve the full 3D structure of the body, we have to use some a priori hypotheses about the shape of the body (e.g., sphere, spheroid, ellipsoid). Moreover, to assess the more probable shape parameters given the sparse data, we adopted a Bayesian approach to derive posterior probability distributions for the radius of the spherical model, and the size, shape, and orientation for the Maclaurin, ellipsoidal, and Jacobi models. The advantage of this method is that it can incorporate knowledge from complementary observations in a quantitative way, avoiding qualitative assumptions (Brown 2013).

In Section 2, we describe the prediction of occultations and the observations, resulting in a total of eight occultation chords observed during five stellar occultations between 2013 and 2016. In Section 3, we describe the rings, main body models, and the implementation of the Markov Chain Monte Carlo (MCMC) to derive parameter values. In Section 4, we describe the main results, before the discussions (Section 5) and concluding remarks (Section 6).

2. Observations

2.1. Prediction of Stellar Occultations

Stellar occultation predictions for Chariklo for the period 2012.5–2014 were based on local catalogs with astrometric positions of the stars around Chariklo's path on the sky. Moreover, improved ephemerides for Chariklo were obtained from those catalogs with typical uncertainties of 20–30 mas (Camargo et al. 2014). A similar approach was used for predictions after 2014 using the Wide Field Imager (WFI) at the MPG 2.2 m telescope (La Silla, Chile) and the IAG 0.6 m telescope at OPD/LNA (Pico dos Dias, Brazil). For the occultation of 2016 October 1, the star position was obtained from *Gaia* Data Release 1 (Gaia Collaboration et al. 2016a, 2016b). A total of 13 positive occultations were observed up to 2016, involving the detection of the rings, the body, or both (see details in Bérard et al. 2017). Each event provided the position of Chariklo relative to the star with an accuracy of a few miliarcseconds. Those positions were used in turn to improve Chariklo's ephemeris, providing updated orbital elements in the so-called Numerical Integration of the Motion of an Asteroid (NIMA) procedure (Desmars et al. 2015), and permitting better subsequent predictions.

2.2. Observations and Data Reduction

Among the 13 stellar occultations observed between 2013 and 2016 (Braga-Ribas et al. 2014; Bérard et al. 2017), we use those five that include the simultaneous detections of the main body and rings. In those cases, the orientation and center of the system can be constrained as detailed in Section 3.1. The 2013 June 3, 2014 June 28, and 2016 October 1 events were double chord while the 2014 April 29 and 2016 August 8 events were single chord. Additionally, we consider the stations whose negative detections (that is, no occultation by the body) were close enough to the main body's limb to constrain its extension. As a consequence, from the occultation of 2013 June 3, we use the negative detections from Ponta Grossa and Cerro Burek (Braga-Ribas et al. 2014); from 2014 April 29, we use a negative detection from Springbok; and from 2014 June 28, we use the negative detection from Hakos. Table 1 gives the circumstances of the observations between 2014 and 2016 used in this work. Details of observations from other sites and stellar occultations not used in this work are given in Braga-Ribas et al. (2014) and Bérard et al. (2017).

For each observation, the images were reduced in a standard way by applying dark and flat frames. Then, we performed aperture photometry for the occulted star and comparison stars in the same image. Finally, we performed relative photometry between the occulted star and comparison star(s) to correct for variations in the sky transparency. The optimal aperture size was chosen in each case for the target and comparison star(s) to obtain the best signal-to-noise ratio (S/N) in each light curve. The background flux was estimated near the target and nearby reference stars, and then subtracted, so that zero flux corresponds to the sky level. The total flux from the unocculted star and Chariklo was normalized to unity after fitting the light curve by a third- or fourth-degree polynomial before and after the event. Figures 1 and 2 show the light curves obtained with this procedure.

2.3. Occultation Timing Analysis

For each light curve involving the body's detection, we determine the times of ingress $t_{\rm ing}$ and egress $t_{\rm egr}$ of the occulted star behind Chariklo by fitting a sharp-edge occultation profile. This profile is convolved by the Fresnel diffraction produced by the sharp edge of the body, then convolved by the stellar diameters projected at Chariklo's distance, the integration time, and the bandwidth of the optical system (product of the telescope, detector, and filter responses) as described in Widemann et al. (2009). The profile takes into account the relative speed of the star with respect to Chariklo in the sky

Table 1
Observations Used to Constrain Chariklo's Main Body

Site	Latitude Longitude Altitude (m)	Telescope Aperture (m) Camera,Filter Exp. Time, Cycle (s)	Observers
2013 June 3, South America[a]			
2014 April 29, South Africa			
Springbok South Africa	29°39′40.″2S 17°52′58.″8W 951	0.3 Raptor Merlin 247, Clear 0.06, 0.06	F. Colas C. de Witt
Gifberg South Africa	31°48′34.″6S 18°46′59.″4E 345	0.3 Merlin, Clear 0.05, 0.05	J.-L. Dauvergne P. Schoenau
South African Astronomical Observatory, Sutherland (SAAO) South Africa	32°22′46.″0S 20°48′38.″5E 1760	1.9 SHOC, Clear 0.0334, 0.04	H. Breytenbach A. A. Sickafoose
2014 June 28, South Africa and Namibia			
Kalahari Trails South Africa	26°46′27″S 20°37′55″E 860	0.3 Merlin, Clear 0.4, 0.4	L. Maquet
Twee Rivieren South Africa	26°28′14″S 20°36′42″E 885	0.3 Merlin, Clear 0.4, 0.4	J.-L. Dauvergne
IAS Observatory Hakos Namibia	23°14′10″S 16°21′42″E 1695	0.51 Merlin, Clear 0.2, 0.2	K.-L. Bath
2016 August 8, Namibia			
Windhoek Namibia	22°41′54.″9S 17°6′32.″4E 1900 m	0.35 ZWO ASI120MM, Clear 1, 1	H.-J. Bode
2016 October 1, Australia			
The Heights Observatory Adelaide Australia	34°48′44.″7S 138°40′56.″9E 100 m	0.3 QHY5L-II, Clear 1, 1	A. Cool B. Lade
Rockhampton Australia	23°16′9.″6S 150°30′0.″7E 50 m	0.3 Watec 910BD, Clear 0.32, 0.32	S. Kerr

Note. The stations considered here involve occultation by Chariklo's main body where Chariklo's rings were simultaneously detected. In those cases, the general geometry of the system can be constrained, including the apparent center and orientation of the pole axis. The Springbok and Hakos stations provided negative results (that is, no occultation by the body), but the occultation chords were sufficiently close to Chariklo's main body, giving strong constrains on its extension (see Figure 3). For the same reasons, we consider in this analysis the observations from the Danish and PROMPT telescopes (body detections) as well as Ponta Grossa and Cerro Burek (no occultation by the body) of the occultation of 2013 June 3.
[a] The circumstances of these observations are given in Braga-Ribas et al. (2014).

plane, v_{ch}, and the orientation angle, α, between the occultation chord and the normal to the local limb. For instance, for a local limb perpendicular to the occultation chord, we have $\alpha = 0$.

The angle α and times $t_{\rm ing}$ and $t_{\rm egr}$ are obtained by minimizing a classical χ^2 function,

$$\chi^2 = \sum_1^N \frac{(\phi_{i,o} - \phi_{i,m})^2}{\sigma_i^2}, \quad (1)$$

where $\phi_{i,o}$ is the normalized flux observed, $\phi_{i,m}$ is the synthetic flux from the diffraction model, and σ_i is the uncertainty in the measured photometry.

Except for the occultation of 2013 June 3 observed with the Danish telescope, the light curves are dominated by the long integration time instead of diffraction effects, so that the angle α is unconstrained and only the ingress and egress times are obtained.

Table 2 gives the adopted stellar diameters projected at Chariklo's distance, Chariklo's geocentric range, the adopted coordinates of the occulted stars, and the predicted coordinates of Chariklo at a reference time. For the occultations of 2014 June 28 and 2016, the apparent stellar diameters are estimated using the V and K apparent magnitudes provided by the NOMAD catalog (Zacharias et al. 2004) using the V–K relations from Kervella et al. (2004) and considering galactic

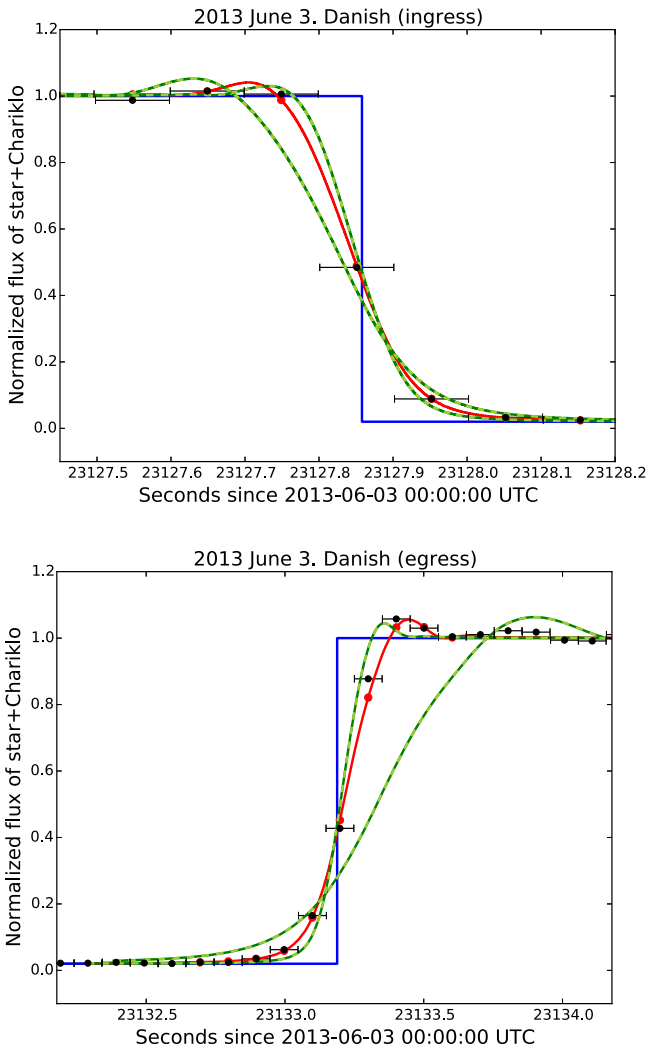

Figure 1. Occultation light curve of 2013 June 3 at the Danish telescope at ingress (top) and egress (bottom). The black dots are the data points with the horizontal bars indicating the time interval of acquisition (the exposure time). The blue continuous line is the geometric best solution indicating the limb of the object, from where we obtain the occultation times given in Table 3. The red continuous line is the best solution after applying the limb diffraction model. The high S/N and cadence of the light curve from the Danish telescope allows the determination of the orientation between the occultation chord and the normal to the local limb, given by the angles $\alpha_{\rm ing} = 60°$ and $\alpha_{\rm egr} = 73°$ at ingress and egress, respectively (see Figure 4). For illustration, the green lines show the limb profiles for $\pm 10°$ with respect to the best-fit values $\alpha_{\rm ing}$ and $\alpha_{\rm egr}$, showing a clear departure from the data (see Section 2.3 for details).

reddening. For 2013 June 3 and 2014 April 29, we adopt the apparent stellar diameter derived in Braga-Ribas et al. (2014) and Bérard et al. (2017).

The occultations by the main inner ring (C1R) and the external fainter ring (C2R) show variable width and radial profiles, and are described and analyzed in detail in Bérard et al. (2017). Here we take the midtimes $t_{\rm mid}$ of the rings' detections from that work, which we use in turn to constrain the body's apparent center as explained in Section 3.1.

The timings corresponding to the occultations by the main body and the rings provide a set of offsets (f, g) of the star with respect to the expected body center as seen from each site. Those offsets are measured in the sky plane at Chariklo's distance, and they are counted positive toward the east and north. Table 3 summarizes the timings and offsets for the body detections, while Table 4 lists the ring detections. Figure 3 shows the occultation chords in the sky plane. The particular conditions during the occultations of 2013 June 3 and 2014 April 29 are discussed below.

South America. 2013 June 3—For this occultation, we keep most of the timing analysis reported in Braga-Ribas et al. (2014), but we re-analyzed the light curve obtained at the Danish telescope. This light curve has the highest S/N and a high acquisition rate of 10 Hz, allowing us to resolve diffraction effects by fitting simultaneously the time of ingress/egress and the orientation angle α.

Figure 1 shows the best fits, from where we derive $\alpha_{\rm ingress} = 60\overset{\circ}{.}2 \pm 0\overset{\circ}{.}9$ at ingress and $\alpha_{\rm egress} = 73\overset{\circ}{.}0 \pm 0\overset{\circ}{.}8$ at egress, while the ingress and egress timings are given in Table 3. For illustration, the same figure indicates the modeled light curve for α departing $\pm 10°$ with respect to the best fit, showing a clear departure from the data.

From this, we calculate the relative angle $\Phi_{\rm limb}$ between the local and global limbs, the latter understood as the tangent to the projected limb. Depending on the main body model, we obtain $\Phi_{\rm limb} = 2°$–$10°$ at ingress and $\Phi_{\rm limb} = 15°$–$25°$ at egress. The angle $\Phi_{\rm limb}$ corresponds to what is known as the angle of internal friction, or the maximum angle of repose. As an illustration, Figure 4 shows a local view of the occultation geometry in the sky plane for the generic triaxial ellipsoid model (Section 3.2.2) indicating the occultation chord, the local limb, the global limb, and the angles α and $\Phi_{\rm limb}$.

Finally, the occultation timings by the main body obtained at the PROMPT telescope (as given by Braga-Ribas et al. 2014), as well as the non-detection at Cerro Burek and Ponta Grossa, are used as further constraints for the overall shape.

South Africa. 2014 April 29—This occultation revealed that the occulted star was in fact double. A stellar atmosphere fit was performed to determine the relative flux and apparent diameter of the stars as detailed in Bérard et al. (2017) The separation between the main (A) and secondary (B) stars, and the diameter of each component projected at the distance of Chariklo are given in Table 2.

The occultation of the primary star by the rings was detected at Springbok, while the occultation of the secondary was not detected due to the low S/N. There were two additional detections of the rings, one involving the C2R ring occulting the primary star at Gifberg and the other one involving the C1R ring occulting the secondary star at SAAO. Panel (b) of Figure 3 shows the two sets of occultations of the primary and secondary stars in the plane of the sky. Panel (c) of Figure 3 shows the reconstructed geometry of the event after applying the offset between the components of the double star to the occultations of the secondary star.

3. Rings and Body Models

3.1. Ring Model

All of the ring occultations observed thus far are consistent with two concentric and circular rings with fixed pole position and fixed radius, within $\sim 1°$ and within ~ 3.3 km of the discovery values, respectively (see Braga-Ribas et al. 2014; Bérard et al. 2017). For a particular date, the rings are projected on the sky plane as an ellipse with semimajor axis corresponding to the ring radius. The ring opening angle B (the elevation of the observer above the ring plane) and the position angle of the semiminor axis P are calculated from the pole

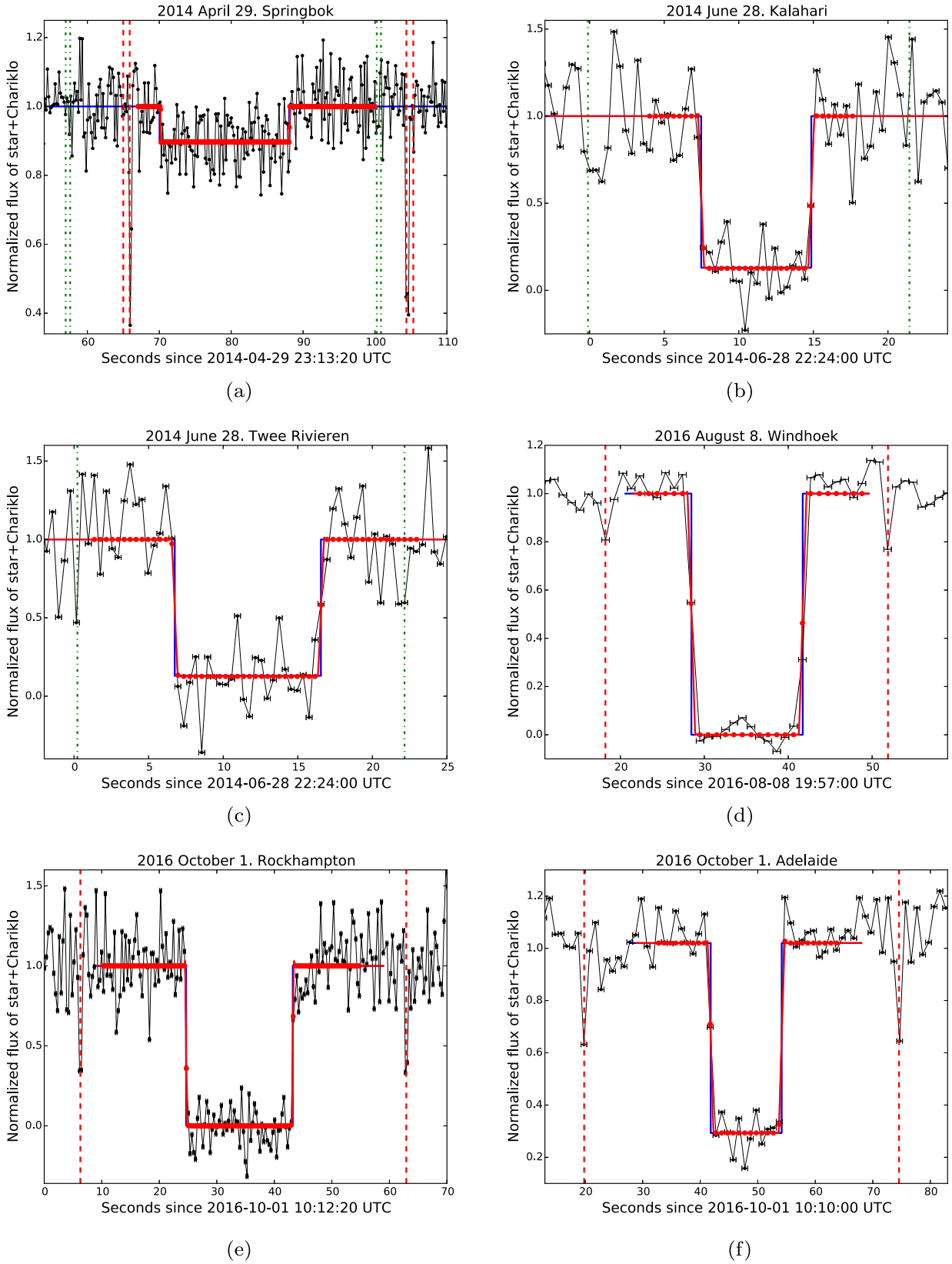

Figure 2. Occultation light curves used in this paper. The black dots are the data points with horizontal bars indicating the time interval of acquisition (the exposure time). The blue continuous lines are the geometric best solution indicating the limb of the object. The red continuous lines are the best solution after applying the limb diffraction model. The red dashed lines show the central times of occultations by the C1R and C2R rings. Notice that only the C1R position is indicated for events with unresolved rings. The green dotted–dashed lines indicate the ring position expected after reconstruction of the geometry of the event in cases where the rings are undetected.

Table 2
Coordinates of Chariklo and the Occulted Star

	2014 Apr 29		2014 Jun 28	2016 Aug 8	2016 Oct 1
α	$17^h39^m2^s.1336$[a]	−10.1 mas[b]	$17^h24^m50^s.3800$	$18^h18^m3^s.6927$	$18^h16^m20^s.0796$
δ	$-38°52'48''.802$[a]	−17.8 mas[b]	$-38°41'5''.618$	$-33°52'28''.3920$	$-33°1'10''.756$
V	…	…	15.20	14.06	14.33
K	…	…	12.47	12.1	13.253
θ_{LD} (mas)	…	…	0.011 ± 0.005	0.015 ± 0.003	0.007 ± 0.002
D_{star} (km)	0.2 ± 0.02[c]	0.09 ± 0.02[c]	0.11 ± 0.05	0.16 ± 0.03	0.08 ± 0.02
t_{ref} UTC	23:10:00		22:24:00	19:57:00	10:10:00
α_{Ch}	$17^h39^m2^s.1566$		$17^h24^m50^s.3991$	$18^h18^m3^s.6908$	$18^h16^m20^s.0982$
δ_{Ch}	$-38°52'48''.739$		$-38°41'5''.628$	$-33°52'28''.241$	$-33°1'10''.8424$
d_{Ch} (km)	2.109×10^9		2.075×10^9	2.193×10^9	2.319×10^9

Notes. (α, δ) are the right ascension and declination of the occulted star, while d_{Ch} is Chariklo's geocentric range and (α_{Ch}, δ_{Ch}) the predicted Chariklo's right ascension and declination at the reference time t_{ref}. V and K are the star magnitudes from the NOMAD catalog (Zacharias et al. 2004). θ_{LD} is the stellar angular diameter, while D_{star} is the stellar diameter projected at the distance of Chariklo, from the V–K relations in Kervella et al. (2004) after considering galactic reddening. For the stellar occultation of 2013 June 3, we adopted values from Braga-Ribas et al. (2014, supplementary information).
[a] Primary component of the double star.
[b] Offset of the secondary component with respect to the primary.
[c] Fitting atmospheric models to primary and secondary stars; for details, see Bérard et al. (2017).

Table 3
Occultation Data Used to Constrains Chariklo's Size and Shape

Site	ing/egr	UTC time	f(km)	g(km)	σ_{ch}(km)[d]
		2013 June 3, South America			
Pta. Grossa[a]	No body detection				
Danish	ing	6:25:27.893 ± 0.014 s	−2750.6	920.2	0.3
Danish	egr	6:25:33.188 ± 0.014 s	−2635.3	898.2	0.3
PROMPT[a]	ing	6:25:24.835 ± 0.009 s	−2842.0	837.7	0.2
PROMPT	egr	6:25:35.402 ± 0.015 s	−2613.3	794.2	0.3
Cerro Burek[a]	No body detection				
		2014 April 29, South Africa			
Springbok[b]	No body detection				
Springbok[c]	ing	23:14:30.04 ± 0.07 s	−2887.6(−2782.6)	321.0(503.0)	0.9
Springbok[c]	egr	23:14:48.05 ± 0.07 s	−2651.3(−2546.3)	373.2(555.2)	0.9
		2014 June 28, South Africa and Namibia			
Hakos	No body detection				
Kalahari	ing	22:24:07.48 ± 0.20 s	−878.6	1306.6	4.4
Kalahari	egr	22:24:14.86 ± 0.07 s	−723.2	1264.2	1.5
Twee Rivieren	ing	22:24:06.73 ± 0.10 s	−892.6	1343.7	2.2
Twee Rivieren	egr	22:24:16.54 ± 0.10 s	−686.3	1287.4	2.2
		2016 August 8, Namibia			
Windhoek	ing	19:57:28.460 ± 0.13 s	631.1	−520.5	2.1
Windhoek	egr	19:57:41.870 ± 0.14 s	831.1	−599.6	2.2
		2016 October 1, Australia			
Rockhampton	ing	10:12:44.66 ± 0.04 s	−497.8	0.4	0.5
Rockhampton	egr	10:13:03.20 ± 0.06 s	−676.7	−149.2	0.8
Adelaide	ing	10:10:41.82 ± 0.10 s	−607.9	124.1	1.3
Adelaide	egr	10:10:54.16 ± 0.08 s	−726.8	25.1	1.0

Notes. Here we list only the positive occultations by Chariklo's body and the negative occultations close enough to the body used to constrain Chariklo's size and shape. The second column indicates the detection of the ingress and egress in Chariklo's occultation shadow at each site. The values (f, g) are the offsets of the star with respect to the expected body center (f, g) = (0,0) as seen from each site at ingress and egress. Those offsets are measured in the sky plane at Chariklo's distance and are counted, respectively, positive toward the east and north.
[a] From Braga-Ribas et al. (2014, extended data Table 5).
[b] Occultation of primary star (see text).
[c] Occultation of secondary star (see text).
[d] The uncertainty σ_{ch} measured in the direction of the occultation chord as derived from the timing uncertainties.

Table 4
Midtime of the Occultations by Chariklo's Rings

Site	ing/egr	t_{mid} UTC	f (km)	g (km)	v_{ch} (km s^{-1})	σ_{ch} (km)
2014 April 29, South Africa						
C1R						
Springbok[a]	ing	23:14:25.884 ± 0.007 s	−2942.16	308.95	13.4	0.1
Springbok[a]	egr	23:15:04.362 ± 0.006 s	−2437.27	420.48	13.4	0.1
SAAO[b]	ing	23:13:56.191 ± 0.007 s	−3017.66	56.58	13.4	0.1
SAAO[b]	egr	23:14:28.964 ± 0.008 s	−2587.52	151.12	13.4	0.1
C2R						
Springbok[a]	ing	23:14:24.990 ± 0.020 s	−2953.89	306.36	13.4	0.3
Springbok[a]	egr	23:15:05.324 ± 0.019 s	−2424.65	423.27	13.4	0.3
Gifberg[a]	ing	23: 14: $30.109^{+0.015}_{-0.008}$ s	−2742.39	137.87	13.4	$^{+0.2}_{-0.1}$
Gifberg[a]	egr	23:14:33.750 ± 0.008 s	−2694.62	148.40	13.4	0.1
2014 June 28, Namibia						
C1R+C2R Unresolved						
Hakos	ing	22:24:25.796 ± 0.041 s	−886.44	1629.24	21.8	0.9
Hakos	egr	22:24:44.218 ± 0.035 s	−498.24	1523.61	21.8	0.8
2016 August 8, Namibia						
C1R+C2R Unresolved						
Windhoek	ing	19:57:18.209 ± 0.249 s	478.18	−459.92	16.0	4.0
Windhoek	egr	19:57:51.892 ± 0.109 s	980.60	−658.82	16.0	1.8
2016 October 1, Australia						
C1R+C2R Unresolved						
Rockhampton	ing	10:12:26.284 ± 0.072 s	−320.56	148.77	12.6	0.91
Rockhampton	egr	10:13:22.928 ± 0.049 s	−876.01	−308.47	12.6	0.62
Adelaide	ing	10:10:19.826 ± 0.186 s	−396.05	300.41	12.5	2.3
Adelaide	egr	10:11:14.558 ± 0.218 s	−923.38	−138.48	12.5	2.7

Notes. C1R is the internal and wider ring, while C2R is the external ring. t_{mid} are the midtimes of the occultations by the rings, from Bérard et al. (2017). Ingress/egress indicates the first and second detection of the respective ring. The values (f, g) are the offsets of the star with respect to the expected body center (f, g) = (0, 0) as seen from each site derived from the midtimes t_{mid}. Those offsets are measured in the sky plane at Chariklo's distance and are counted, respectively, positive toward the east and north. v_{ch} is the speed of the star relative to Chariklo, projected in the sky plane. σ_{ch} is the uncertainty of the chord extremity measured along the chord direction as given by the timing uncertainty.
[a] Occultation of primary star (see text).
[b] Occultation of secondary star (see text).

position in Table 5 and Chariklo's position in the sky. The single-chord ring occultation of 2016 August 8 provides two possible ring centers, while the other events give a unique center. The ring centers (f_c, g_c) are listed in Table 5, with error bars that reflect the uncertainties on the ring midtimes given in Table 4. Occultations indicate that the radial width of the main ring varies between 5 and 7.5 km, adding an additional bias in the determination of the center of ∼1 km. This is of the order of the formal uncertainties for most of the events, and it is not a dominant effect in the determination of the center of the projected ellipse. The best fitted ellipses for each event are displayed in Figure 3.

3.2. Body Model

Here we adopt the assumption that the ring system lies in the equatorial plane of the object. Indeed, in this situation, a collisional dissipative ring reaches its minimum energy configuration while conserving its angular momentum parallel to the body spin axis. With this assumption (plus the circularity described above), the body and the rings share the same pole position and the same center.

If Chariklo were completely irregular, a simple parametric model (e.g., sphere, ellipsoid) would give a poor estimation of the dimensions of the body. A well-sampled stellar occultation could indicate if Chariklo is irregular but unfortunately, to date we only have a few occultations with one or two positive detections each (Table 3 and Figure 3). In that context, we test simple models that can be easily parametrized in order to give credible intervals for the corresponding parameters. In practice, we first assume a spherical body that is used to estimate a radius and the scale of the topographic features. Next, we consider a generic triaxial ellipsoid to estimate the length of the semiaxes a, b, and c, and the scale of the topographic features. Next, considering hydrostatic equilibrium, a homogeneous body will assume either a Maclaurin (spheroid) or a Jacobi (triaxial ellipsoid) shape for which size, axis ratios, density, and topographic features can be evaluated. The non-spherical models incorporate independent information as a priori estimates for the model parameters, such as the amplitude of the rotational light curve or the long-term photometric behavior of the system. The models mentioned above (sphere, triaxial ellipsoid, Maclaurin, and Jacobi) are now discussed in turn.

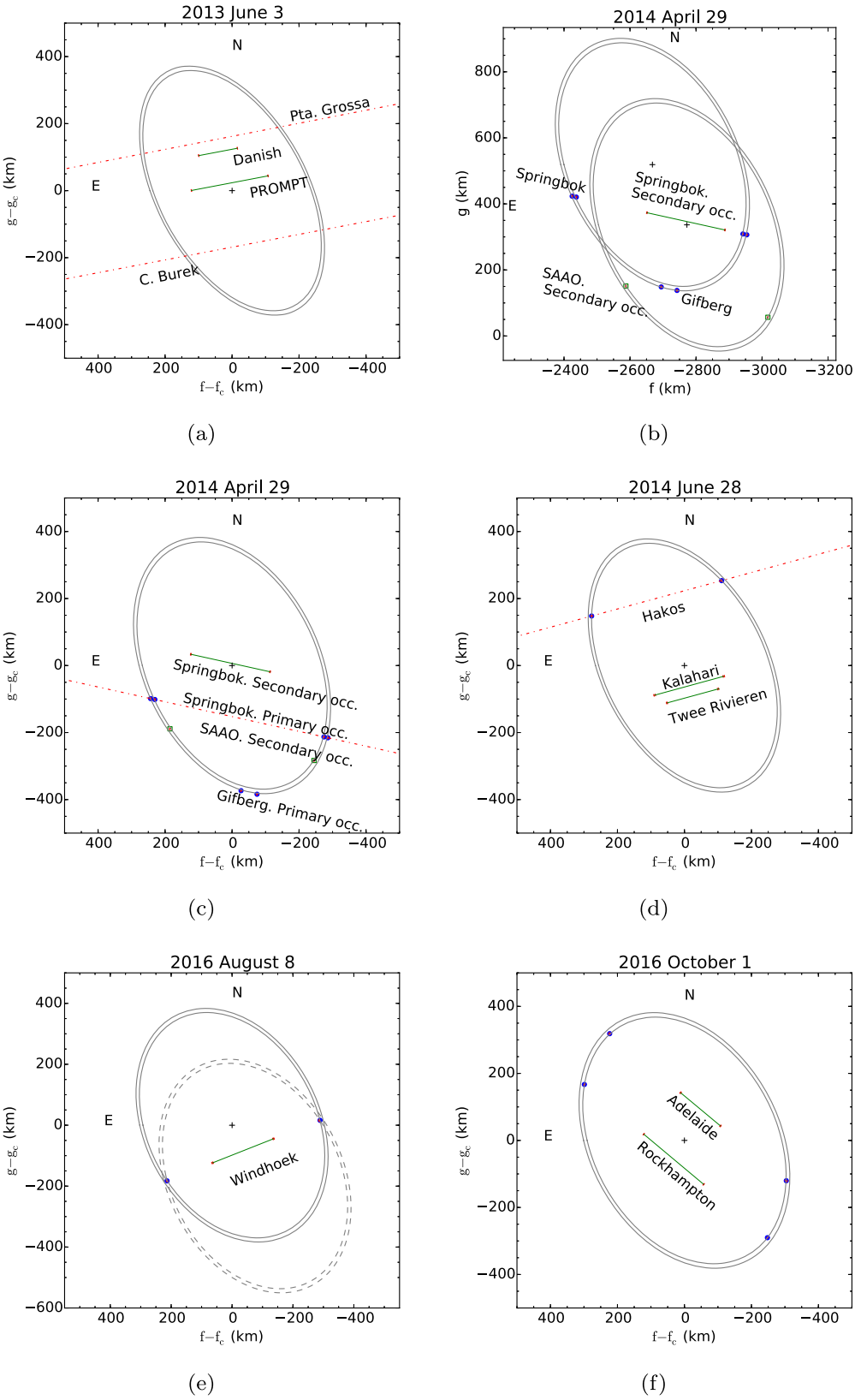

Figure 3. Geometry for the five occultations by Chariklo's main body between 2013 and 2016. Positions are given in the sky plane at Chariklo's distance with respect to the center of the system (f_c, g_c) determined in Table 5. The ellipses represent the C1R and C2R orbits adopting the diameter and pole position of Braga-Ribas et al. (2014). Dots indicate the ring detections used to fit the center of the system (black crosses). The continuous green lines are the occultation chords by the main body with the uncertainties in red. For clarity, we only indicate the closest negative detections used as constraints with the red dotted–dashed lines. (a) 2013 June 3, South America. (b) 2014 April 29, South Africa. Occultation of a double star. The solid dots and the cross indicate the ring occultation of the primary star and the adopted center of the system. Open dots correspond to occultations of the secondary star. (c) 2014 April 29, South Africa. Geometry after applying an offset of $\Delta f = 103$ km and $\Delta g = 182.5$ km to the secondary events. (d) 2014 June 28, South Africa–Namibia. (e) 2016 August 8, Namibia. Rings solution 1 in continuous line and solution 2 in dashed lines. (f) 2016 October 1, Australia.

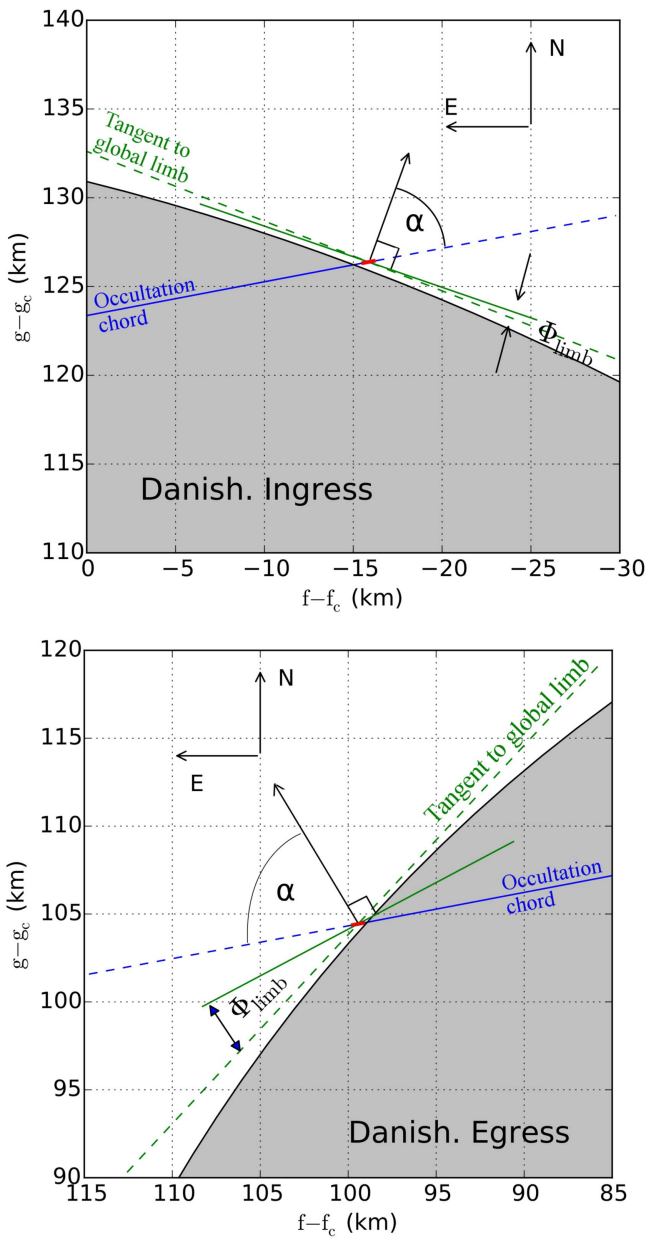

Figure 4. Local limb slopes with respect to the generic ellipsoid model as measured at the Danish telescope for the occultation of 2013 June 3. The tangent to the local limb (solid green line) is derived from fitting the angle α in the limb diffraction model to the occultation light curves (Figure 1). The blue solid lines are the occultation chords with their extremity uncertainties in red. Depending on Chariklo's main body model, the slopes with respect to the tangent to the global limb of up to $\Phi_{\rm limb} = 25°$ are observed. As an illustration, this figure shows the local limb orientation for the generic ellipsoidal model.

3.2.1. Sphere Model

This is the simplest case as there is only one free parameter, the sphere radius R. The projection in the sky plane is a circle with the same radius R for all occultations. The problem is then reduced to finding a circle that best fits all of the chord extremities (f, g) provided in Table 3 with the center located at the (f_c, g_c) values indicated in Table 5.

3.2.2. Triaxial Ellipsoid

Here we consider a generic triaxial ellipsoid with semiaxes $a > b > c$, rotating around the shortest axis. We define the rotation angle ϕ as the angle from the central meridian to the prime meridian counted positively along the equator of the object using the right-hand rule. The prime meridian is the one passing through one of the two intersections between the equator and the longer axis of the ellipsoid. Given the current uncertainty in the rotation period, the rotation phase is lost after a few weeks, and the rotation angle in each occultation is considered to be independent.

The eight free parameters of this model are a (which gives us the size of the object), the ratios $0 < b/a < 1$ and $0 < c/b < 1$, and the rotation angles ϕ_i at each of the five occultations.

3.2.3. Maclaurin Spheroid

A Maclaurin spheroid has an equatorial radius a and polar radius c related by (Chandrasekhar 1987)

$$\Omega = \frac{\omega^2}{\pi G\rho} = \frac{2\sqrt{1-e^2}}{e^3}[(3-2e^2)\arcsin e - 3e\sqrt{1-e^2}], \tag{2}$$

where $e^2 = 1 - (c/a)^2$, $\omega = 2\,\pi/T$ (T being the rotation period of the body), G the gravitational constant, and ρ its (uniform) density. Note that Ω is the adimensional rotational parameter that compares the centrifugal acceleration at the equator of the body to its gravity. For stable Maclaurin shapes, this parameter is between $\Omega = 0$ and $\Omega \simeq 0.374$. The lower limit corresponds to the spherical limit with $\rho \to \infty$, while the upper limit corresponds to the maximum oblateness and the minimum density. Here we adopt a rotation period of $T = 7.004$ hr (Fornasier et al. 2014), giving a minimum density

$$\rho_{\rm min} = 791 \text{ kg m}^{-3}. \tag{3}$$

In this case, we have two free parameters, the equatorial radius a and the density ρ (which determine c, i.e., the shape).

3.2.4. Jacobi Ellipsoid

A Jacobi ellipsoid is triaxial with semiaxes $a > b > c$, rotating around the shortest axis. The shape and size (given by a, b, and c), the rotation period T, and the (uniform) density ρ are related by (Chandrasekhar 1987)

$$\begin{aligned}\Omega = \frac{\omega^2}{\pi G\rho} &= 2abc\int_0^\infty \frac{u}{(a^2+u)(b^2+u)\Delta}du \\ &\times a^2b^2\int_0^\infty \frac{du}{(a^2+u)(b^2+u)} = c^2\int_0^\infty \frac{du}{(c^2+u)\Delta} \\ \Delta &= \sqrt{(a^2+u)(b^2+u)(c^2+u)}\,,\end{aligned} \tag{4}$$

which can be solved numerically.

For a stable Jacobi ellipsoid, the shapes lie between the axisymmetric spheroid limit with $\Omega = 0.374$ and the most elongated solution with $\Omega = 0.284$. For the adopted rotation period of 7.004 hr, the density is in the range $791 < \rho < 1040$ kg m^{-3}.

We define the prime meridian and rotation angle ϕ as we did for the generic ellipsoid.

The seven free parameters of this model are a (which gives us the size of the object), the density ρ (which gives us the

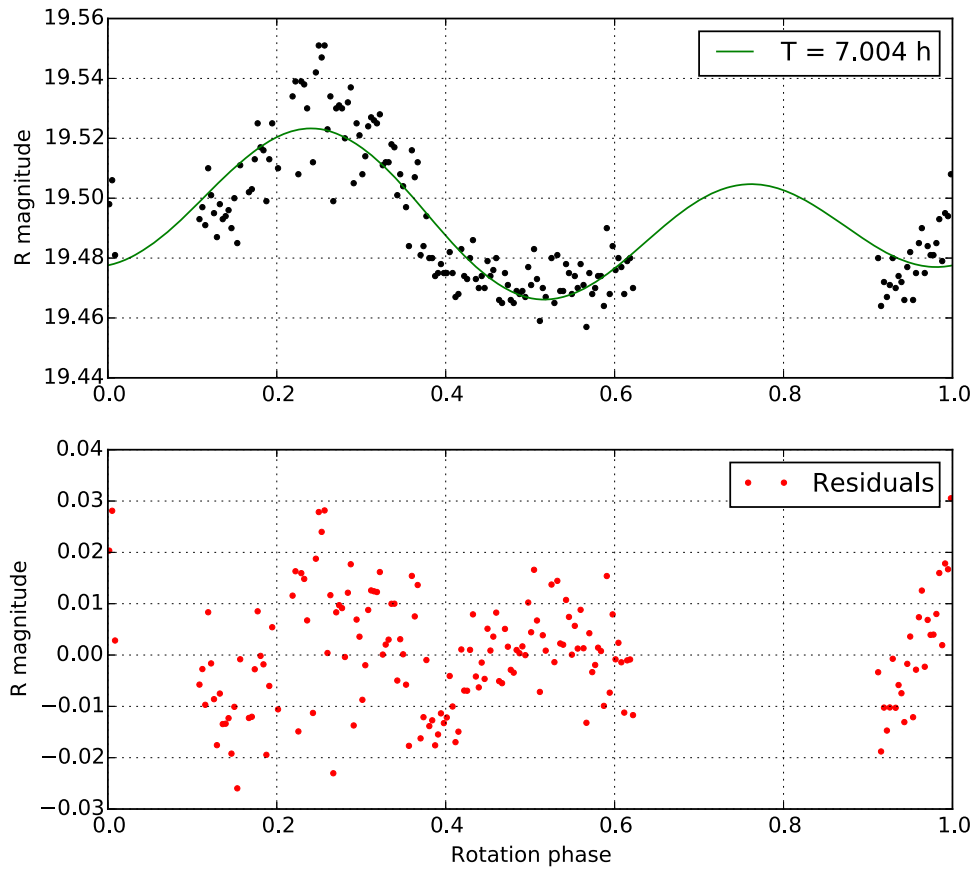

Figure 5. Chariklo's rotational light curve obtained on 2015 July 20 with the SOI camera at SOAR telescope. The light curve covers about 5 hr of Chariklo's rotation. The green solid line is a fit with a second-order polynomial after folding the data with a period $T = 7.004$ hr from Fornasier et al. (2014). The peak-to-peak amplitude from this light curve is $\Delta m = 0.06 \pm 0.02$ mag. Using the pole position from Table 5, the opening angle of Chariklo's system at this date is $B = 42°$. Together with the Δm and H_V values from the literature, this is used to derive a prior for the size and shape of the models.

Table 5
Adopted Ring Geometry

Pole position[a]	$\alpha_P = 151.°30 \pm 0.°5$ and $\delta_P = 41.°48 \pm 0.°2$			
C1R radius[a] (km)	390.6 ± 3.3			
C2R radius[a] (km)	404.8 ± 3.3			
Date	Opening Angle—B (°)	Position Angle—P (°)	f_c (km)	g_c (km)
2013 Jun 3[a]	33.8 ± 0.4	−61.6 ± 0.1	−2734.7 ± 0.5	793.8 ± 1.4
2014 Apr 29	40.4 ± 0.4	−64.5 ± 0.4	−2669.4 ± 0.2	519.0 ± 0.1
2014 Jun 28	37.8 ± 0.4	−63.1 ± 0.4	−775.3 ± 0.5	1375.8 ± 0.5
2016 Aug 8[b]	45.2 ± 0.4	−62.9 ± 0.4	767.1(691.7) ± 4.0	−475.95(−642.8) ± 7.0
2016 Oct 1	44.5 ± 0.4	−62.0 ± 0.4	−619.3 ± 1.0	−17.8 ± 3.4

Notes. The opening angle B is the elevation of the observer above the ring plane. P is the position angle of the semiminor axis of the ring projected on the sky plane, counted positively from celestial north toward east. With the assumptions used here, B and P correspond to the planetocentric declination of the Earth and the position angle of the pole axis, respectively (see Section 3). f_c and g_c are the coordinates of the center of the ring in the sky plane measured with respect to the expected body center $(f, g) = (0, 0)$.
[a] From Braga-Ribas et al. (2014), ED Table 4.
[b] For the occultation of 2016 August 8, there are two possible solutions for the center of the system.

shape with Equation (4)), and the rotation angles ϕ_i at each of the five occultations.

3.3. Bayesian Approach and MCMC Implementation

Here, we adopt a Bayesian approach to derive the probability densities and credible intervals for the physical parameters θ of the models described above given the occultation data D. We are interested in the "posterior" probability density function (pdf) $p(\theta|D)$ given by

$$p(\theta|D) \propto \mathcal{L} \times p(\theta), \tag{5}$$

where $\mathcal{L}$ is the likelihood function and $p(\theta)$ is the so-called "prior" distribution.

Table 6
Rotational Light Curve Amplitudes

Date	Δm (mag)	B (°)	Reference
1997 May	<0.02	−56	Davies et al. (1998)
1999 Mar	<0.05	−53	Peixinho et al. (2001)
2006 Jun	0.13 ± 0.03	−13	Galiazzo et al. (2016)
2013 Jun	0.11 ± 0.02	34	Fornasier et al. (2014)
2015 Jul	0.06 ± 0.02	42	This work

Note. Peak-to-peak amplitude Δ_m of the rotational light curve measured for Chariklo at different opening angles B. Upper limits for the amplitude in 1997 and 1999, and uncertainties in 2006 and 2013 are estimated from the uncertainties in the photometry given by the authors. The amplitude in 2015 is the one obtained from data taken with the SOI camera at the SOAR telescope.

The likelihood $\mathcal{L}$ determines the probability of obtaining the data D given the physical model and a model of the data uncertainties. On the other hand, the prior distribution $p(\theta)$ condenses the previous knowledge we have about the parameters. We define the likelihood function $\mathcal{L}$, assuming that the errors stemming from the fits described in Section 2.3 have normal distributions. Moreover, we formally consider statistical uncertainties in our model by introducing an extra, normally distributed random variable with median zero and standard deviation σ_m, independent from the measurements. For instance, the parameter σ_m may account for unmodeled topographic features on an otherwise smooth ellipsoidal model for the body. Thus, σ_m is estimated from the data and counted as an extra parameter for each physical model. With these considerations, $\mathcal{L}$ is given by (see for example Equation (4.52) of Gregory 2005)

$$\mathcal{L} = (2\pi)^{-N/2}\left\{\prod_{i=1}^{N}(\sigma_{ri}^2+\sigma_m^2)^{-1/2}\right\} \times \exp\left\{-\sum_{i=1}^{N}\frac{(y_i - m(x_i|\theta))^2)}{2(\sigma_{ri}^2+\sigma_m^2)}\right\}, \quad (6)$$

where N is the number of data points $y_i = (f_i, g_i)$ derived in Section 2.3, corresponding to the extremities of each occultation chord by the main body; x_i represent the independent variables (the site and time of each occultation); and σ_{ri} are the uncertainties on the chord extremities σ_{ch} projected along the radial direction and counted from the center (f_c, g_c) of the body (see Table 5). Finally, θ is the vector representing the parameters of the model that describes the object. In that context, $m(x_i|\theta)$ is the position of the chord extremity predicted by each model. The prior $p(\theta)$ is derived from physical considerations (for instance, the stability criteria for the Maclaurin and Jacobi models) and the observational evidence as explained below.

3.3.1. Analysis of Photometry

Here we consider the rotational light curve amplitude Δm and V absolute magnitude H_V, which are in turn used to derive a priori estimates for Chariklo's size, shape, and/or density, depending on the model adopted. These a priori estimates are incorporated in the Bayesian modeling through the prior probability distribution $p(\theta)$.

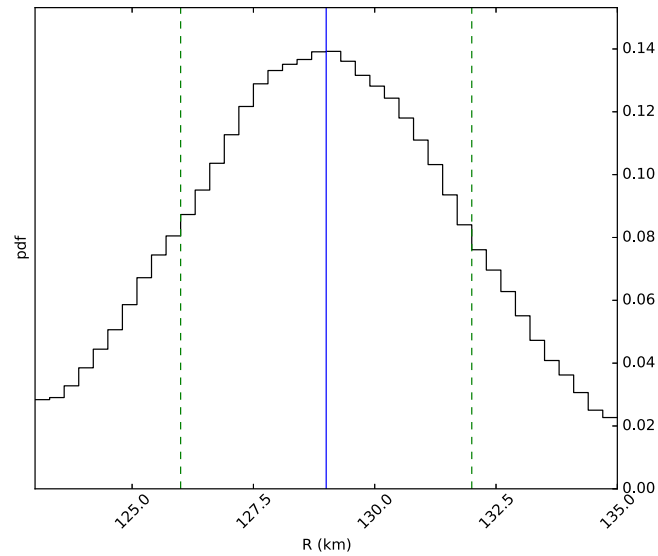

Figure 6. Posterior probability function (pdf) for the sphere radius R. The blue continuous line is the best value, and the green dashed lines indicate the 68% credible interval from where we determine the value for $R = 129 \pm 3$ km.

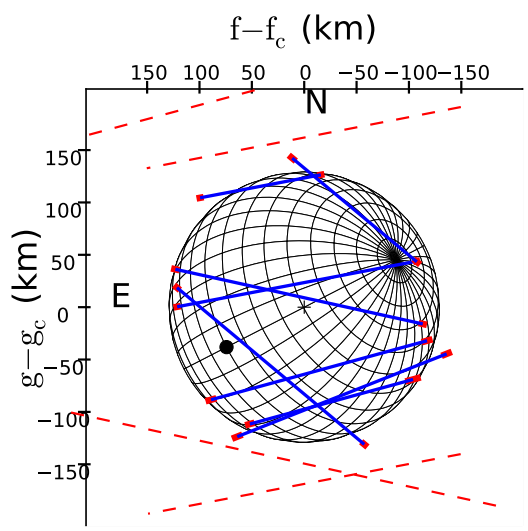

Figure 7. Best fit for the sphere model with radius $R = 129 \pm 3$ km compared to all of the occultation chords projected on the sky plane. The sphere model is plotted with the average orientation of $B = 40°$ and $P = -63°$. Measurement uncertainties are indicated in red. The red dashed lines outside the body are the multiple negative detections used to constrain the model. The black dot indicates the sphere's equator.

Notice that in this discussion we neglect the effect of eclipses between the main body and the rings. For instance, for a spherical body with radius $R = 129$ km, eclipses between the body and the main ring C1R occur for opening angles $\lesssim 20°$. The projected area of the ring eclipsed by Chariklo's main body is $\lesssim 10\%$ of the total ring projected area, while the projected area of the main body eclipsed by the rings is $\lesssim 1\%$ of the total body projected area. Both effects are negligible compared to the uncertainty in the ring's width of $\sim 20\%$ (Bérard et al. 2017). Moreover, none of the stellar occultations analyzed in this work involve eclipses.

Rotational light curve amplitude—Chariklo exhibits a rotational light curve amplitude that varies in time. There was

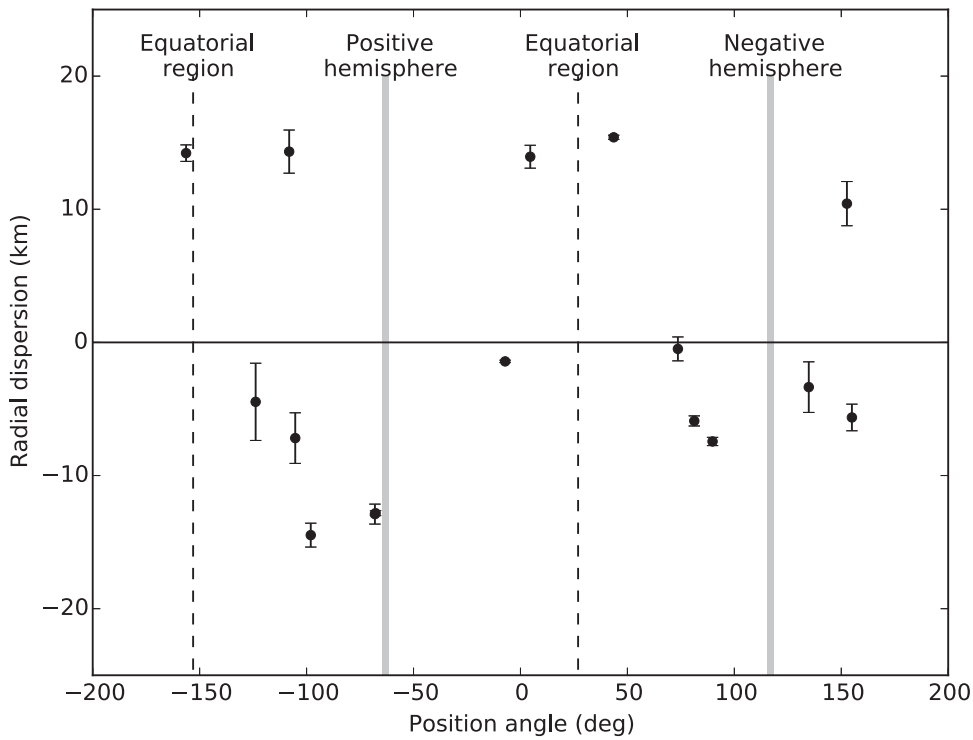

Figure 8. Radial residual as a function of position angle (counted positively from celestial north toward east) for the spherical model of Figure 7. Error bars are the uncertainties in the position of the occultation chord extremities projected in the radial direction. Dashed lines indicate the equatorial region while the solid lines indicate the polar region. Positive and negative hemispheres are defined according to the choice of the pole position given in Table 5. We observe a clear correlation of the radial residuals with the position angle along the limb, with positive residuals in the equatorial region and negative residuals in the polar regions.

no detection of the light curve amplitudes obtained in 1997 and 1999 (Davies et al. 1998; Peixinho et al. 2001), when Chariklo was close to its maximum opening angle. Peak-to-peak amplitudes of 0.13 mag and 0.11 mag were then measured in 2006 and 2013, respectively (Fornasier et al. 2014; Galiazzo et al. 2016). As not given by the authors, we adopt conservative upper limits for the amplitudes in 1997 and 1999, and uncertainties for those of 2006 and 2013, derived from the uncertainties in the respective photometries.

Here we add to this data set a partial light curve obtained in July 2015 with the SOAR Optical Imager (SOI). About 200 images were taken with the R Bessell filter using an exposure time of 80 s. A bias correction and flat-fielding was performed with the SOAR/SOI IRAF routines. The images were processed using the difference image photometry implemented in the IDL code DanDIA (Bramich 2008). A light curve was obtained using aperture photometry with IRAF routines (Tody 1986). Figure 5 shows the obtained light curve covering ~5 hr from which we determined a peak-to-peak amplitude $\Delta m = 0.06 \pm 0.02$.

Values from the literature and from this work are summarized in Table 6. Using the pole position from Table 5, we calculate the opening angle B for each date that indicates a correlation between Δm and $|B|$. Additionally, the light curve from Fornasier et al. (2014) is double peaked, with the minima separated by about half of the rotation phase. Both facts suggest that the brightness variations are dominated by the variable projected area of an elongated body instead of albedo variegations.

With these considerations, we model the peak-to-peak rotational light curve amplitude with the contribution of the main body and rings given by (Fernandez-Valenzuela et al. 2017)

$$\Delta m = -2.5 \log\left(\frac{A_{\min} p_b + A_r (I/F)}{A_{\max} p_b + A_r (I/F)}\right), \tag{7}$$

where $A_{\min}$ and $A_{\max}$ are the minimum and maximum projected areas of Chariklo's body, respectively, p_b is the geometric albedo of Chariklo's body, A_r is the projected area of the rings, and[26] (I/F) is the ring reflectivity.

Absolute magnitude—Chariklo also exhibits an absolute V magnitude H_V that varies in time (Belskaya et al. 2010; Duffard et al. 2014; Fornasier et al. 2014). Considering contributions from the changing aspect of Chariklo's main body and its rings, we model H_V with the relation

$$H_V = H_\odot - 2.5 \log\left(\frac{A_b\, p_b + A_r\, (I/F)}{\pi\ \mathrm{au}_{\mathrm{km}}^2}\right), \tag{8}$$

where $H_\odot = -26.74$ is the absolute magnitude of the Sun in V, A_b is the projected area of Chariklo's main body, and $\mathrm{au}_{\mathrm{km}}$ is an astronomical unit in km.

Priors for the generic ellipsoid—For the generic triaxial ellipsoid, we use Δm and H_V to derive estimates for the semimajor axis a and the ratios b/a and c/a.

To derive the ring contribution to the brightness variations, we consider a ring of radius ~400 km and width w_1 ~5.5 km (neglecting the contribution from the faint and narrow C2R ring), and a ring reflectivity (I/F) varying between 0%

[26] Here, I is the intensity emitted by the ring surface and πF is the incident solar flux density. The quantity I/F must not be confused with the geometric albedo of the ring particles p_p.

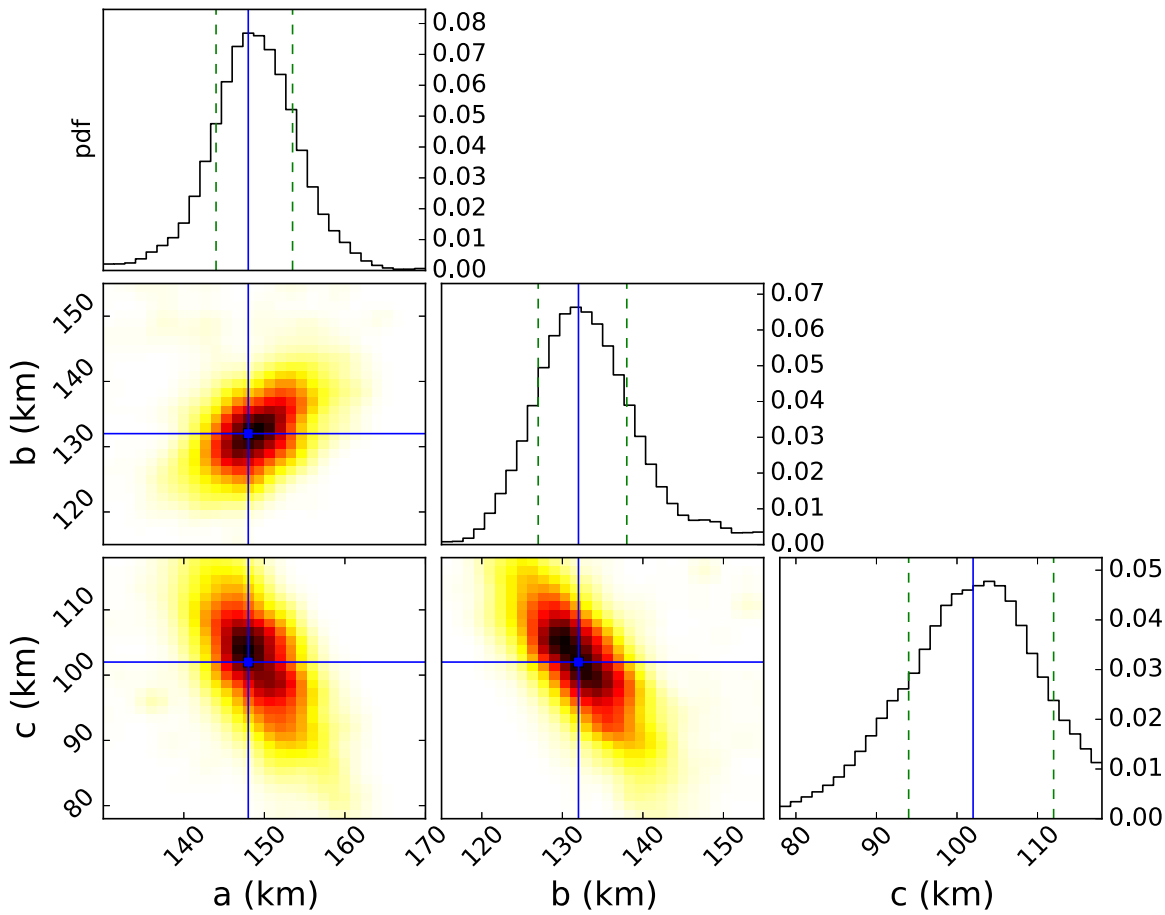

Figure 9. Results for the generic triaxial ellipsoid. The plots in the diagonals show the marginal posterior pdf $p(\theta|D)$ (Equation (5)) for the semiaxes a, b, and c. The rest of the plots are the joint posterior pdf for a vs. b (left-center), a vs. c (bottom-left), and b vs. c (bottom-center). The blue continuous lines indicate the best-fit values adopted, and the green dashed lines indicate the 68% credible intervals given in Table 7.

(neglecting the ring contribution) up to 9%, considering previous estimations of this quantity (Braga-Ribas et al. 2014; Duffard et al. 2014). For the body's contributions, we adopt a body geometric albedo $p_b = 4.2\% \pm 0.5\%$ from Fornasier et al. (2014),

We fit the Equations (7) and (8) to the Δm values in Table 6 and H_V from the literature in a least-squares scheme, obtaining

$$a = 138 \pm 16\ \mathrm{km},\ \frac{b}{a} = 0.86 \pm 0.04,\ \frac{c}{b} = 0.89 \pm 0.30, \tag{9}$$

which are used in Section 4.2 to define normally distributed priors for those parameters.

Priors for the Maclaurin spheroid—For the Maclaurin model, we use H_V values to derive estimates for the equatorial radius $a = b$ and the density ρ. Adopting the same ring dimensions, body geometric albedo, and range of ring reflectivity as before, we fit Equation (8) to the H_V from the literature in a least-squares scheme to obtain

$$a = b = 135 \pm 25\ \mathrm{km}, \tag{10}$$

while we find that the density ρ is unbounded and can take values in all valid intervals between $\rho = 791\ \mathrm{kg\ m^{-3}}$ and $\rho \to \infty$.

In practice, we consider a conservative upper limit for the density

$$\rho_{\max} = 5000\ \mathrm{kg\ m^{-3}}, \tag{11}$$

after considering the known density distribution of asteroids and TNOs (Britt et al. 2002; Carry 2012).

These values are used in Section 4.3 to define normally and uniformly distributed priors for those parameters.

Priors for the Jacobi ellipsoid—For the Jacobi ellipsoid, we must impose the binding conditions from Equation (4) on a, b, and c. As done with the generic ellipsoid, we fit the Equations (7) and (8) to the Δm and H_V values to obtain

$$a = 151 \pm 13\ \mathrm{km},\ \rho = 804 \pm 6\ \mathrm{kg\ m^{-3}}. \tag{12}$$

which is used to define the normally distributed priors in Section 4.4.

Rotation angle during occultations—It is worth mentioning here some words about the rotation angle during the stellar occultations. The rotation light curve from Fornasier et al. (2014) was obtained in 2013 between June 11 and June 12. Assuming that most of the variability is due to the shape instead of albedo variegations, we define the rotation angle $\phi = 0°$ at one of the brightness minima of that light curve, for instance, JD = 2456455.23. This is used to determine the rotation angle $\phi(\mathrm{JD}, T_{\mathrm{sid}})$ at any given date JD for a given sidereal rotation period T_{sid}. For instance, for the stellar occultation of June 3, which is only eight days before this

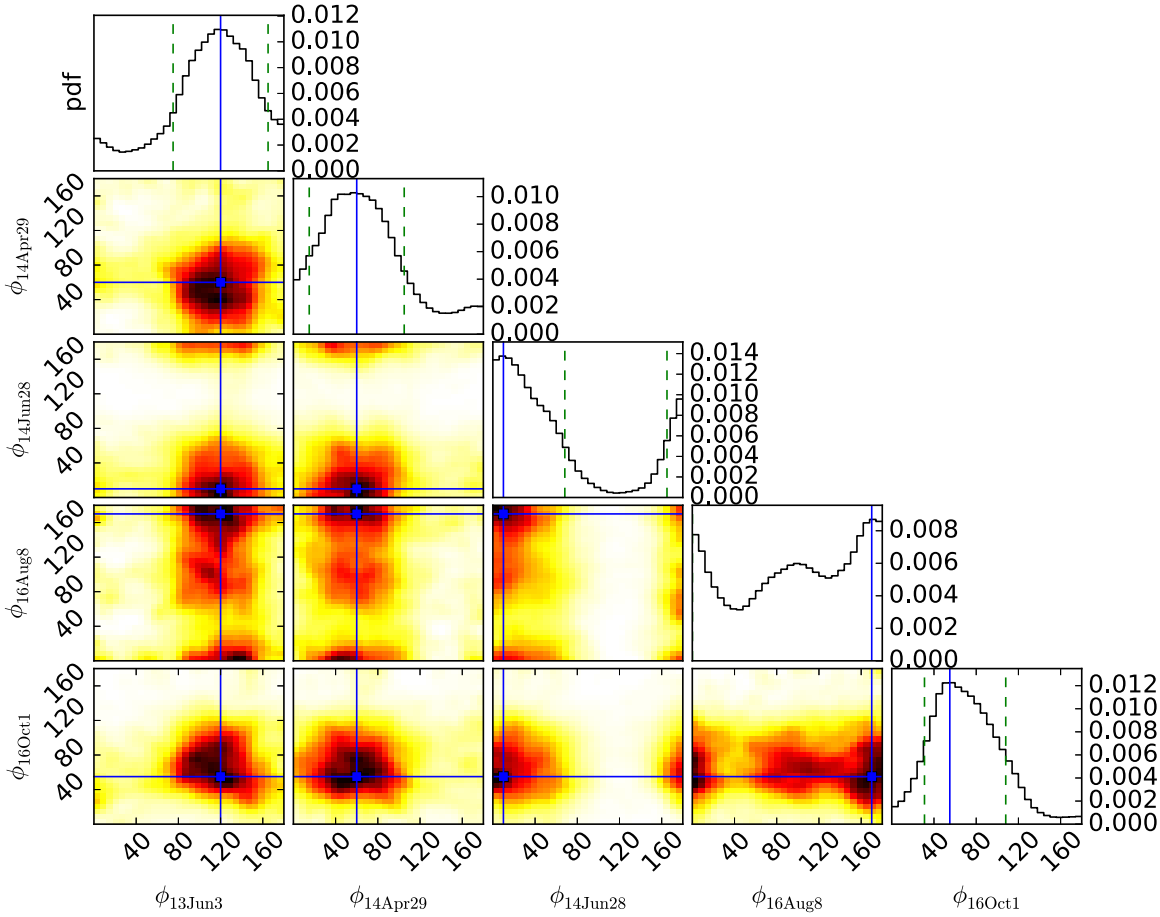

Figure 10. Posterior pdf of the rotation angle ϕ for each occultation for the generic ellipsoid model. The best-fit values used in Figure 11 are indicated by the blue dots and lines. Green dashed lines indicate the 68% credible intervals, except for the occultation of 2016 August 8, where the rotation angle pdf is multimodal. For August 8, the two peaks in the pdf are due to the single chord. Each peak in the pdf occurs when the body limb is roughly equidistant from the chord extremities.

Table 7
Physical Parameters of Chariklo from Stellar Occultations

Parameter	Sphere	Maclaurin	Ellipsoid	Jacobi
ρ(kg m^{-3})	…	970^{+300}_{-180}	…	796^{+2}_{-4}
a(km)	129 ± 3	143^{+3}_{-6}	148^{+6}_{-4}	157 ± 4
b(km)	129 ± 3	143^{+3}_{-6}	132^{+6}_{-5}	139 ± 4
c(km)	129 ± 3	96^{+14}_{-4}	102^{+10}_{-8}	86 ± 1
R_{equiv} (km)	129 ± 3	126 ± 2	126 ± 2	123^{+3}_{-1}
σ_m (km)	11	7	6	6
d_{rms} (km)	10	7	5	5
d_{max} (km)	+15	+11	+12	+9
Mass (kg)	…	$8 \pm 1 \times 10^{18}$	…	$6.1 \pm 0.1 \times 10^{18}$
p_b (%)	3.1 ± 0.1	3.8 ± 0.1	3.7 ± 0.1	4.2 ± 0.1
I/F (%)	8.9 ± 0.3	3.4 ± 0.3	4.9 ± 0.3	0.6 ± 0.4

Note. Best parameter values and formal uncertainties from the 68% credible intervals obtained with the prior as defined in Section 3.3.1. See Section 4 for the sensitivity of the results to the priors chosen. d_{rms} is the rms dispersion in the radial direction with respect to the nominal body limb. d_{max} is the maximum distance in the radial direction with respect to the nominal body limb. p_b is the geometric albedo of the body, while I/F is the ring reflectivity considering only the main ring with width $W = 5.5$ km (not to be confused with the geometric albedo of the ring particles p_p) as determined in Section 5.2. $R_{\mathrm{equiv}} = (a \times b \times c)^{1/3}$ is the volumetric equivalent radius.

measurement, we find

$$\phi_{2013\mathrm{Jun03}} = 356^\circ \pm 54^\circ, \tag{13}$$

adopting $T_{\mathrm{sid}} = 7.004 \pm 0.036$ hr. Unfortunately, given the current accuracy of the rotation period, the rotation angle is essentially lost after a few weeks, preventing us from deriving a rotation angle for the occultations in 2014 and 2016 solely from the light curve in Fornasier et al. (2014). The rotation angle in the ellipsoidal and Jacobi models is then considered independent between occultations and explored between 0° and 180° due to the rotational symmetry.

3.3.2. MCMC Scheme

To estimate the posterior probability distribution $p(\theta|D)$, we adopt an MCMC scheme to draw samples from it. The MCMC sampling is done using the library emcee (Foreman-Mackey et al. 2013), which implements the affine-invariant ensemble sampler by Goodman & Weare (2010).

To generate the posterior samples, we follow a standard procedure. For each model, we run an MCMC with n_{walk} random "walkers," each of them exploring the parameter space. To determine the number of random steps n_{burn} necessary to ensure chain convergence, we adopt $n_{\mathrm{burn}} > 10 \times \tau_f$, where τ_f

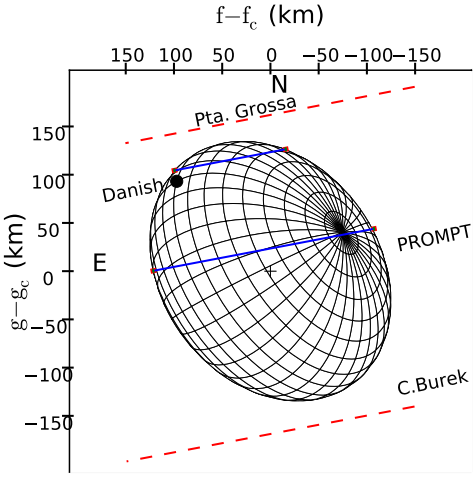

(a) 2013 June 3

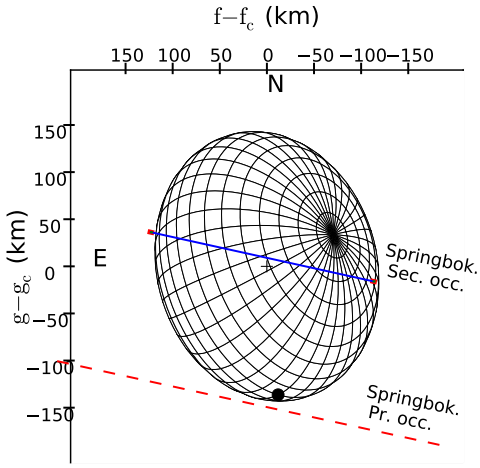

(b) 2014 April 29

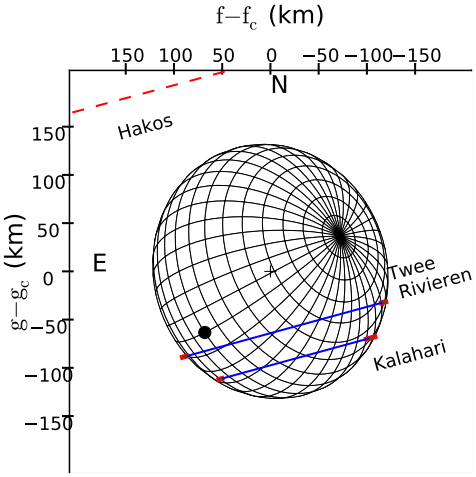

(c) 2014 June 28

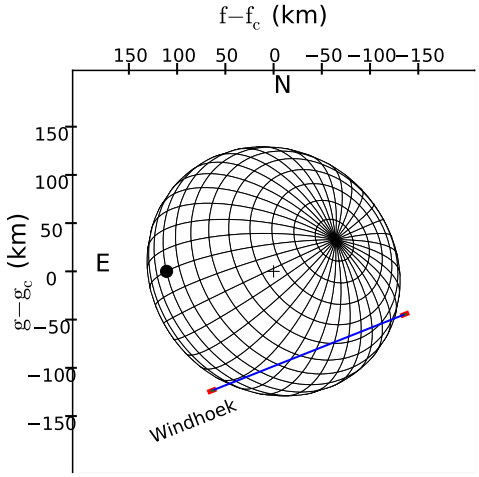

(d) 2016 August 8

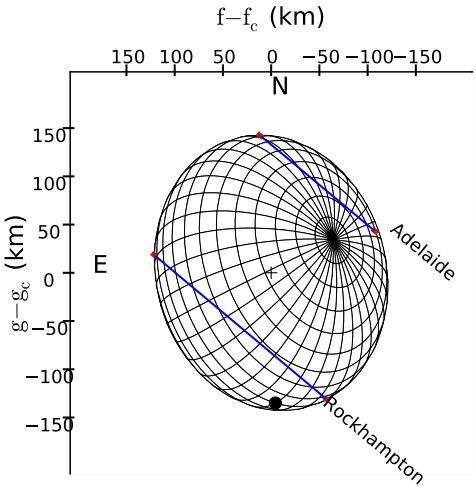

(e) 2016 October 1

Figure 11. Results of the triaxial model using the best-fit values in Table 7. At each panel, the body has the same pole position (α_P, δ_P) and apparent center (f_c, g_c) as the rings (not shown) as given in Table 5. Blue lines are the detections of the main body with uncertainties in red. Red dashed lines are the negative chords closest to the object used as constraints for the body model. The black dot indicates the intersection between the equator and the prime meridian, which is used as the reference to define the rotation angle ϕ.

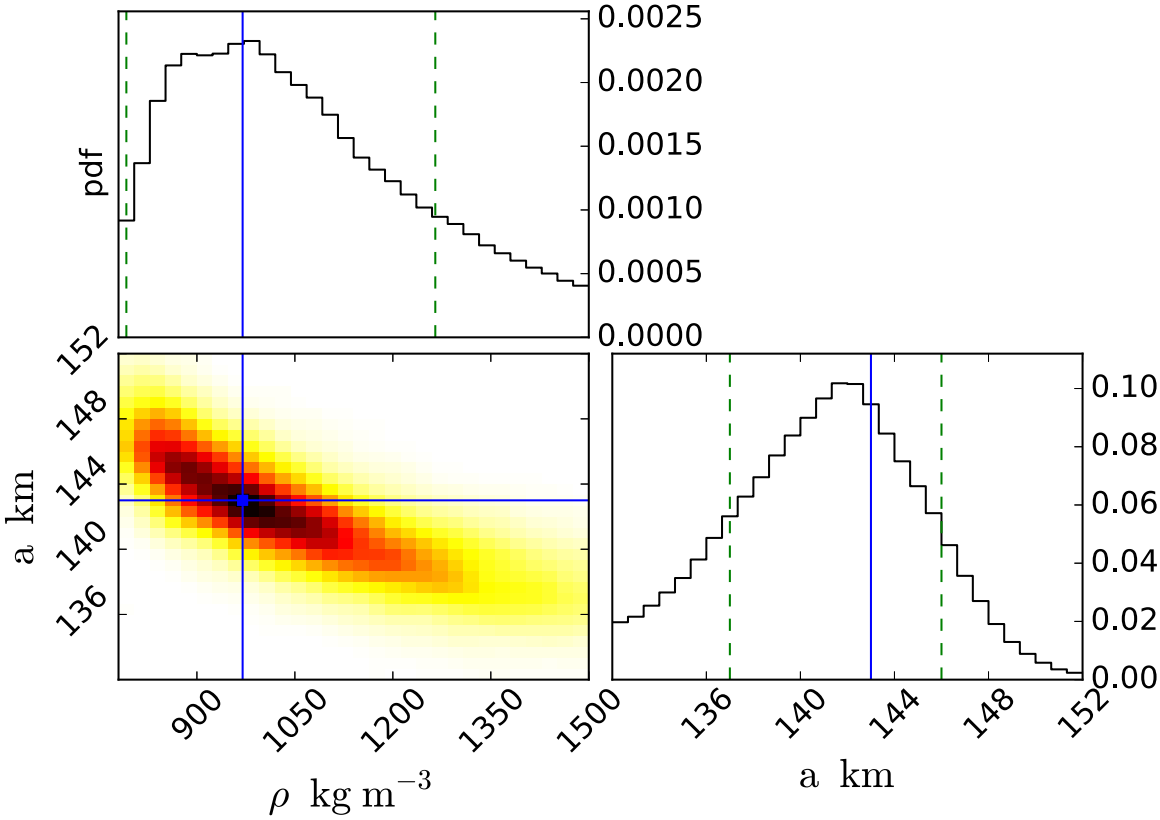

Figure 12. Results for the Maclaurin spheroid model. Bottom left: the joint posterior probability $p(\theta|D)$ (Equation (5)) for the density ρ and equatorial radius a. Top left: the marginal posterior probability for the density ρ. Bottom right: the marginal posterior probability for the equatorial radius a. The blue continuous lines indicate the best parameter values, and the dashed vertical lines indicate the 68% credible intervals given in Table 7.

is the integrated autocorrelation "time" of the chain measured in chain steps (Foreman-Mackey et al. 2013; for this we use the implementation given in emcee). Once this is done, we continue the MCMC for $n_{\rm samp}$ steps, from which we obtain the samples that are representative of the posterior probability of interest $p(\theta|D)$. Then, the marginal probability distribution for the parameters θ is estimated using the histograms of the samples. From the histograms, we derive the best-fit parameter values and credible intervals. For the credible intervals, we use the highest posterior probability density interval containing 68% of the samples. This is the smallest interval such that any point inside the interval has a higher probability density than any other point outside of the interval.

Additionally, and as a heuristic test for convergence, for each model, we run several chains starting with $n_{\rm walk}$ walkers at different random positions well spread in the parameter space. We repeat this procedure several times to verify that we obtain the same results.

4. Occultation Results

4.1. Sphere

For the spherical model, we use as a prior a uniform distribution between $R = 100$ and $R = 150$ km, and for σ_m we adopt a uniform distribution between 0 km and 50 km. Using $n_{\rm walk} = 500$, $n_{\rm burn} = 10^4$ steps, and $n_{\rm samp} = 10^2$ steps, we obtain the posterior pdf shown in Figure 6, and eventually a sphere radius of $R = 129 \pm 3$ km (68% credible interval).

For the best-fit radius, we obtain a "topographic" parameter $\sigma_m = 11$ km. That is, the radial departures from the best-fit limb can be modeled as normally distributed with a standard deviation of 11 km, which is ~9% of the radius R.

In Figure 7, we compare all of the occultation chords with the best fitted limb using the spherical model. In Figure 8, we plot the radial difference of each chord extremity with respect to the best limb as a function of the position angle (counted positively from the north toward the east). There is a clear tendency for the chord extremities to be inside the sphere limb around the polar regions and outside the limb in the equatorial regions. As the departures are significantly larger than the uncertainties on the data points, this naturally motivates us to test the flattened models below.

4.2. Triaxial Ellipsoid

For the triaxial ellipsoid model, we use normally distributed priors for a, b/a, and c/b with values from Equation (9). The normal distributions are truncated such that $a > 0$ and the ratios b/a and c/b stay in the open interval]0,1[, keeping the condition $a > b > c$. For σ_m, we adopt a uniform distribution between 0 km and 50 km as with the previous model. Finally, for the rotation angles ϕ_i, we adopt uniform distributions between 0° and 180°. We do not explore the range 180°–360° due to the rotational symmetry of the ellipsoid.

Using $n_{\rm walk} = 500$, $n_{\rm burn} = 10^4$, and $n_{\rm samp} = 10^2$, we obtain the posterior pdf for a, b, and c shown in Figure 9, and the posterior for the rotation angles shown in Figure 10, from

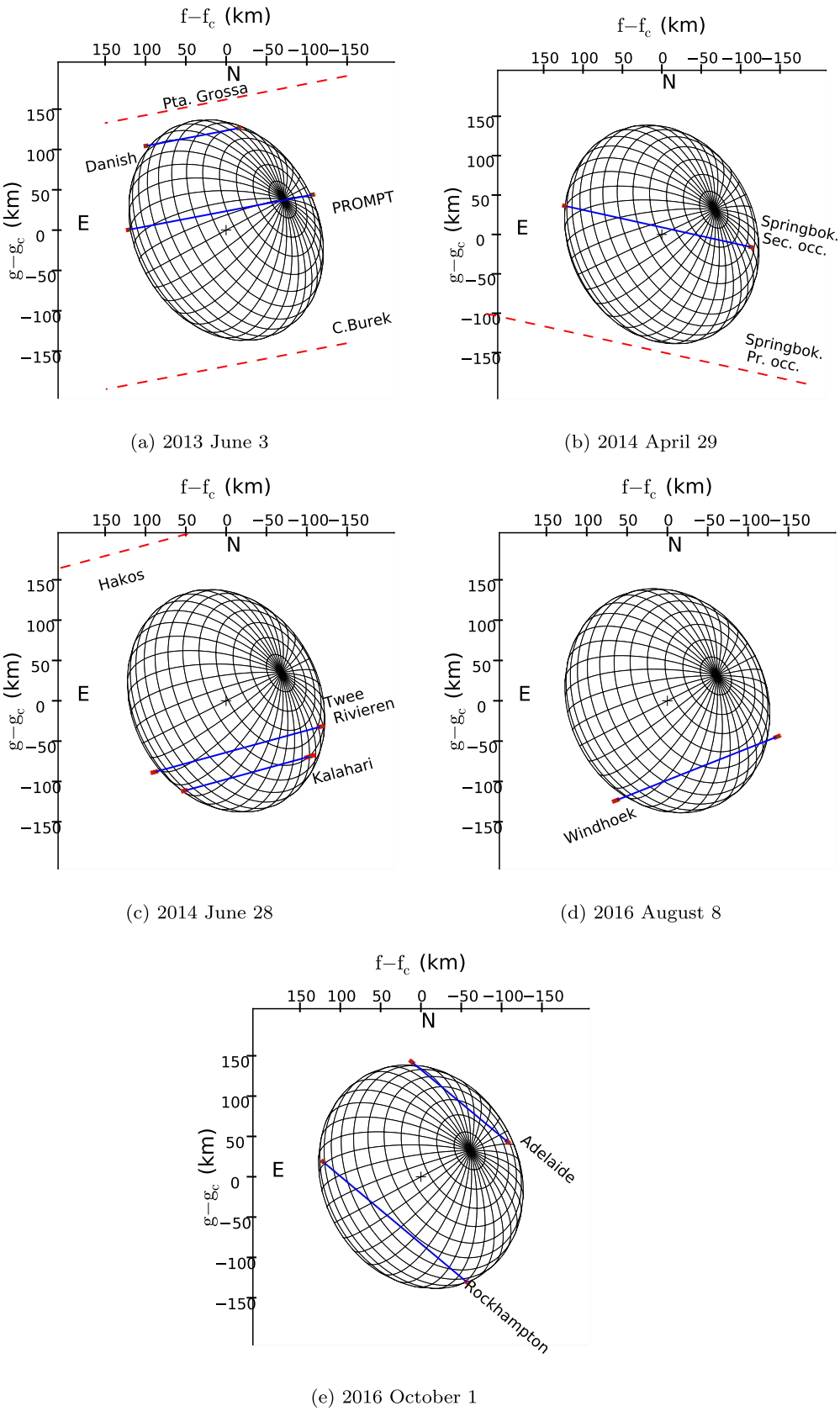

(a) 2013 June 3

(b) 2014 April 29

(c) 2014 June 28

(d) 2016 August 8

(e) 2016 October 1

Figure 13. Same as Figure 11 for the Maclaurin model using the best-fit values in Table 7.

which we determine the parameter values given in Table 7. Figure 11 shows the best-fit ellipsoid models compared to the occultation chords.

From Figure 10, we obtain a rotation angle $\phi = 120° \pm 45°$ for the occultation of 2013 June 3. Considering the ellipsoid rotational symmetry, this angle is equivalent to $\phi = 300° \pm 45°$,

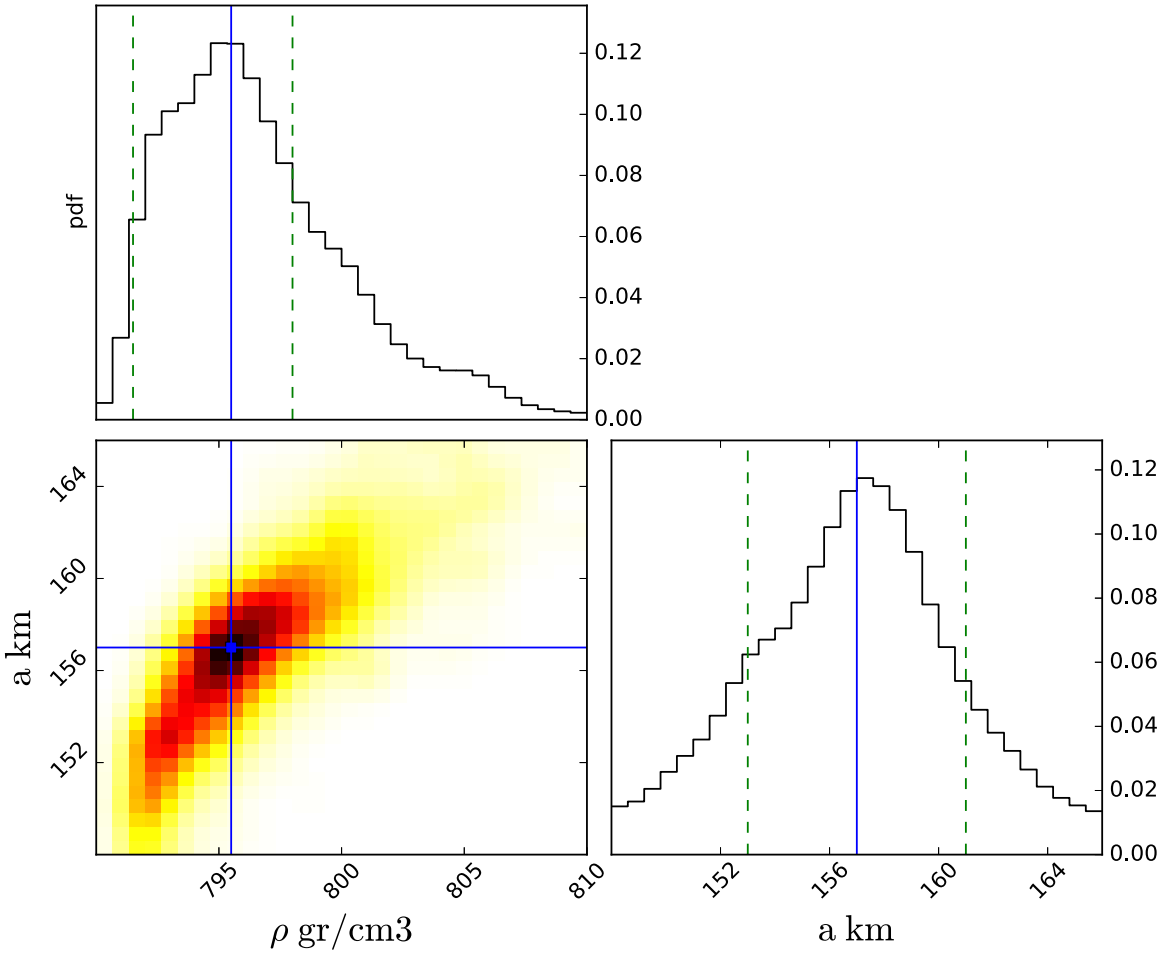

Figure 14. Same as Figure 12 for the Jacobi ellipsoid model, from which we obtain the parameter values given in Table 7.

consistent with the one obtained from the rotational light curve in Section 3.3.1. This validates the assumption that the short-term variability is dominated by the projected shape of a rotating elongated body rather than albedo features.

Sensitivity to priors—To test the sensitivity to priors, we repeat an MCMC run with uniform distribution between 100 km and 200 km for the semimajor axis a, and uniform distribution between 0.1 and 1 for the ratios b/a and c/b. In this case, we determine $a = 147^{+7}_{-3}$ km, $b = 139 \pm 6$ km, and $c = 98^{+9}_{-8}$ km.

This indicates that the priors have some influence in the results, particularly in the ratio $b/a = 0.95$, which is larger than above. Nonetheless, the parameters obtained are mainly dominated by the occultation data.

4.3. Maclaurin Spheroid

For the prior in the density ρ, we use a uniform distribution with values from Equations (3) and (11). For the equatorial radius $a = b$, we use a normally distributed prior with values from Equation (10). Using $n_{\rm walk} = 500$, $n_{\rm burn} = 10^4$, and $n_{\rm samp} = 10^2$, we obtain the posterior pdf for ρ and a shown in Figure 12. We take the maximum of the joint distribution of ρ and a as the most probable values, while the formal uncertainties are taken from the 68% credible intervals from which we obtain the values given in Table 7.

From the joint posterior in the lower-left panel of Figure 12, we note that ρ and a are correlated. For lower densities, the hydrostatic equilibrium figure is more flattened, and consequently, a larger object is needed to match the occultation data.

The upper "wing" for larger densities in the posterior pdf is due to the relation between density and oblateness (Equation (2)). As the density increases, the oblateness changes more slowly, and the body asymptotically approaches a sphere for $\rho \to \infty$.

Figure 13 shows the nominal Maclaurin solution compared to the occultation chords. As with the ellipsoidal case, the parameter $\sigma_m = 7$ km is smaller than that for the spherical model.

Sensitivity to priors—As done with the ellipsoidal model, we repeat an MCMC run using a uniformly distributed prior for the equatorial radius a between 100 and 150 km. From the posterior distribution of ρ and a, we obtain $\rho = 950^{+300}_{-150}$ kg m^{-3} and $a = 144 \pm 4$ km, showing that the results are not strongly sensitive to the priors chosen and are dominated by the occultation data.

4.4. Jacobi Ellipsoid

For the Jacobi ellipsoid model, we use normally distributed priors for the semimajor axis a and density ρ with values from Equation (12). Additionally, the density must satisfy the

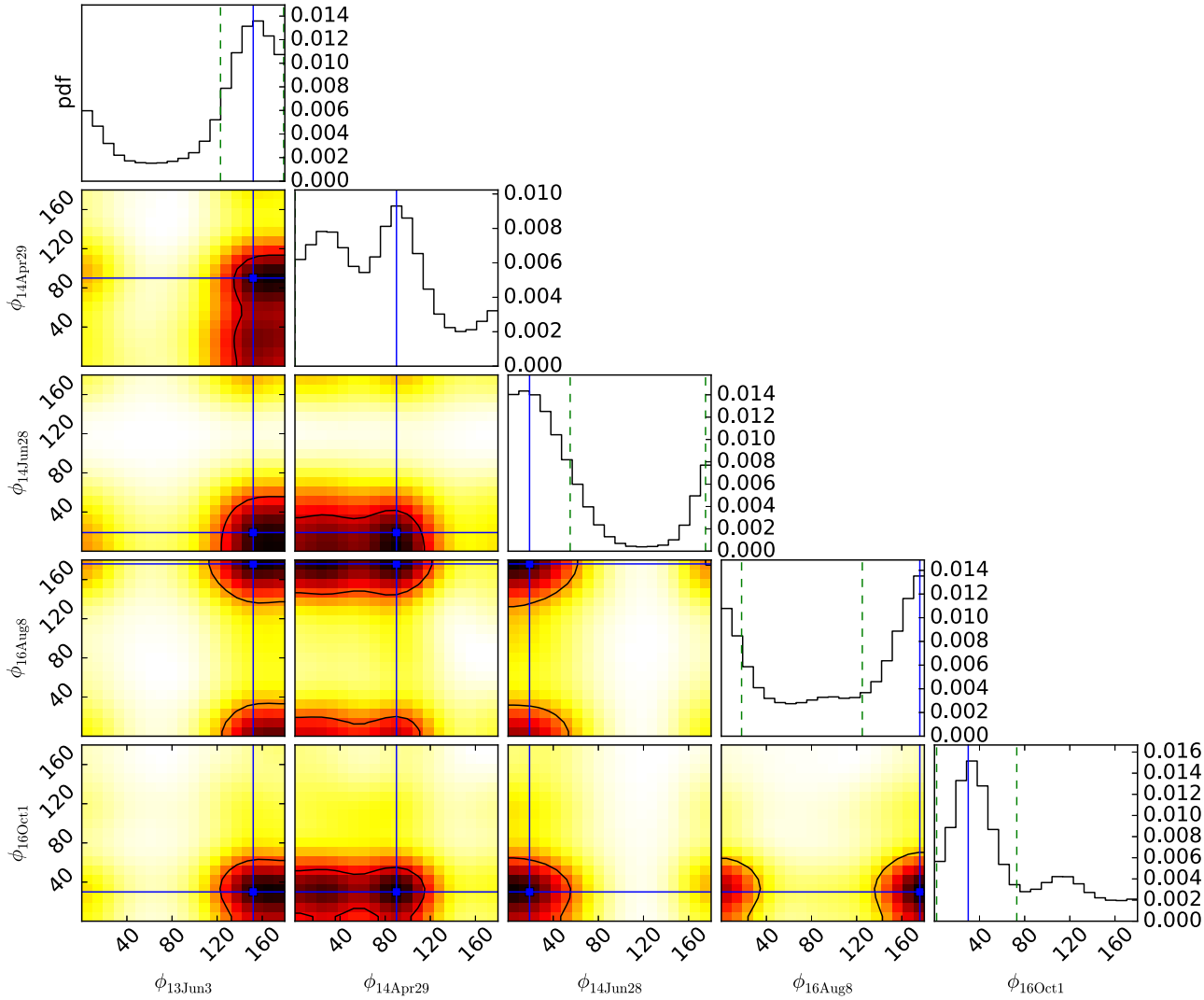

Figure 15. Posterior probability of the relative rotation angle ϕ for each occultation. The best-fit values used in Figure 16 are indicated by the blue dots and lines.

condition of equilibrium as described in Section 3.2, which is $791 < \rho < 1040\,\mathrm{kg\,m^{-3}}$.

Using $n_{\mathrm{walk}} = 500$, $n_{\mathrm{burn}} = 10^4$, and $n_{\mathrm{samp}} = 10^2$, we obtain the posterior pdf for ρ and a shown in Figure 14, and the posterior for rotation angles shown in Figure 15. From this and Equation (4), we derive the parameter values given in Table 7.

Figure 16 shows the best-fit Jacobi models compared to the occultation chords. The scattering of the data points with respect to the best-fit limb is given by $\sigma_m = 6$ km, similar to the case of the Maclaurin model. From Figure 15, we obtain the rotation angle $\phi = 152° \pm 20°$ for the occultation of 2013 June 3. Considering the ellipsoid rotational symmetry, this angle is consistent with the one obtained from the rotational light curve in Section 3.3.1.

Sensitivity to priors—As done with the ellipsoidal and Maclaurin models, we repeat an MCMC run using a uniformly distributed prior between 100 and 150 km for the semimajor axis a, and between 791 and $1040\,\mathrm{kg\,m^{-3}}$ for the density ρ (the equilibrium condition from Section 3.2). We obtain a density $\rho = 792^{+4}_{-1}\,\mathrm{kg\,m^{-3}}$ and semiaxes $a = 152 \pm 5$ km, $b = 144^{+3}_{-4}$ km, and $c = 86^{+2}_{-1}$ km. This is similar to the results above, with a slightly smaller object but with the same elongation ($a - b$), showing that, as with the other models, the results are dominated by the occultation data.

5. Discussion

5.1. Topographic Features and Hydrostatic Equilibrium

The "topographic" parameter σ_m (ranging from 6 to 11 km, depending on the model) indicates the degree of irregularity of the surface. Compared to the equivalent radius for each model, this irregularities are in the range 5%–9%. Moreover, the limb slopes measured in 2013 at one station (Section 2.3 and Figure 4) may reach 25°, measured with respect to the tangent of the global object limb.

Note that Iapetus, with a typical density of $1100\,\mathrm{kg\,m^{-3}}$, can sustain slopes greater than 30° (Castillo-Rogez et al. 2007) while being more massive than Chariklo. Similarly, Hyperion's limb profiles show local slopes of up to 20°, with respect to the fitted elliptical limb (Thomas 1989). More generally, Hyperion is irregular with topographic features of rms ∼12% with respect to the mean radius, while Phoebe is close to a spheroid

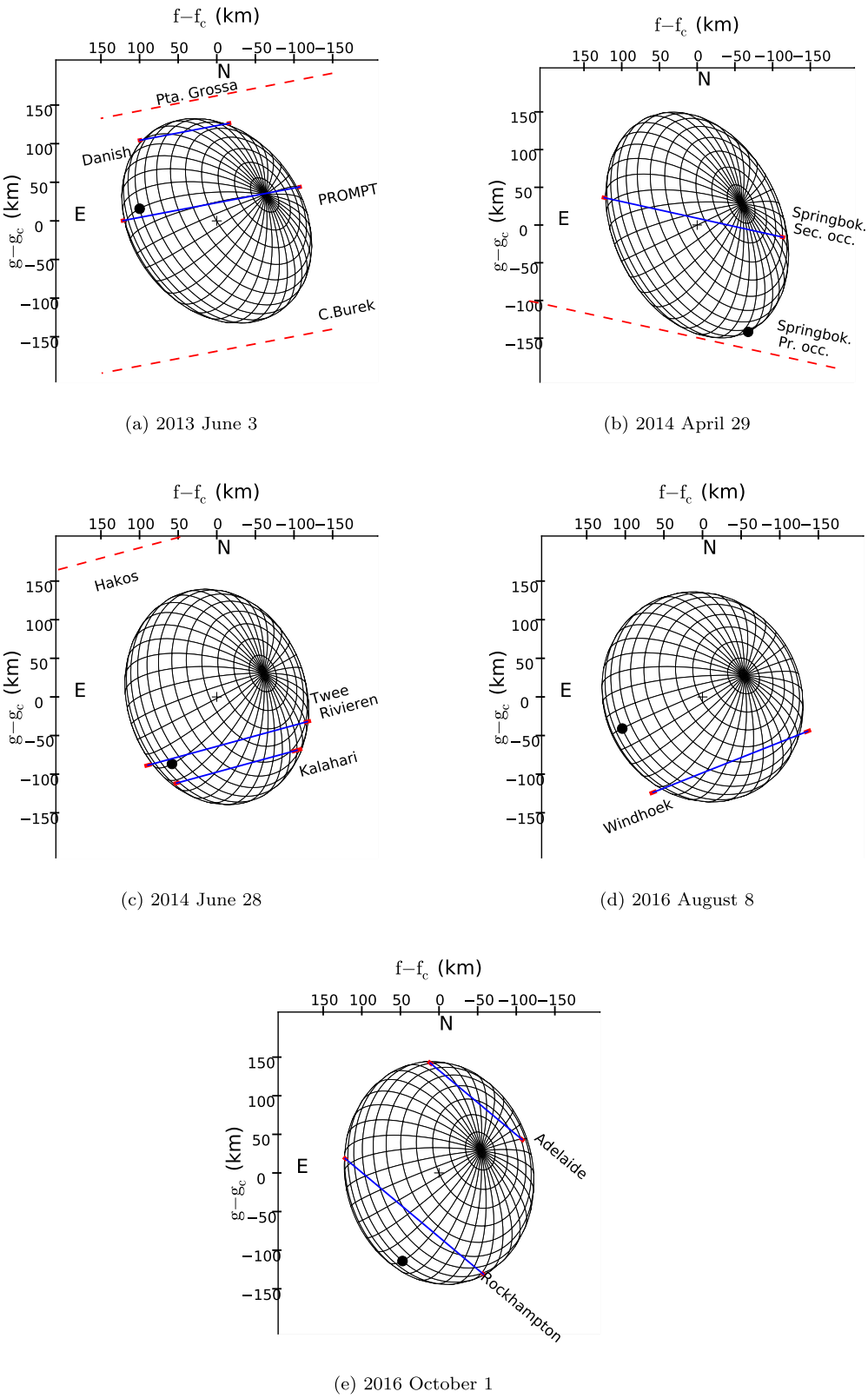

(a) 2013 June 3

(b) 2014 April 29

(c) 2014 June 28

(d) 2016 August 8

(e) 2016 October 1

Figure 16. Same as Figure 11 for the Jacobi model with the best-fit values from Table 7.

in equilibrium with features of rms $\sim$ 5% (Castillo-Rogez et al. 2012), both comparable to $d_{\rm rms}$ values given in Table 7.

In summary, the topographic features and slopes found for Chariklo are typical of small icy satellites with size and density in the same range as Chariklo.

5.2. Body Albedo and Rings Reflectivity

We proceed to evaluate the geometric albedo p_b of Chariklo and the ring reflectivity I/F (see Section 3.3.1), considering the long-term brightness variations of Chariklo. We use the absolute V magnitude H_V from the literature and the same

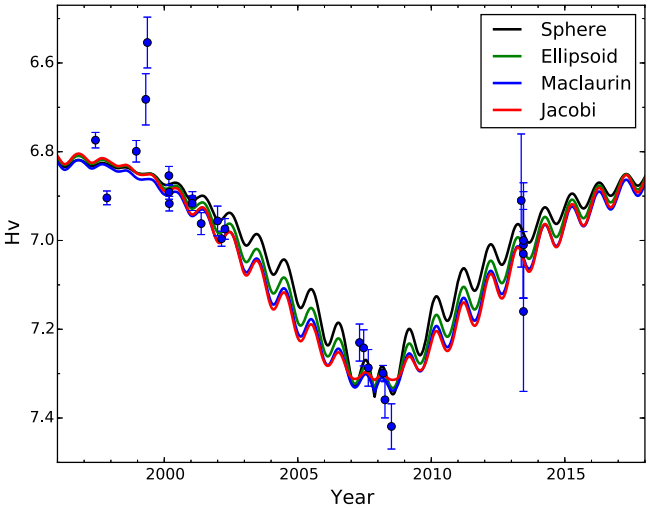

Figure 17. Best-fit to the V absolute magnitude H_V of Chariklo's system. The main body geometric albedo p_b and ring reflectivity I/F are fitted with a least-squares fit to the H_V values from the literature (Belskaya et al. 2010; Fornasier et al. 2014; Duffard et al. 2014). In the extreme case of the spherical model, all of the brightness variations are due to the change in the rings' aspect angle, with $I/F = 8.9\%$. On the other hand, the change in the projected area of the Jacobi model explains most of the long-term brightness variations, resulting in very dark rings with $I/F = 0.6\%$. The Maclaurin and generic triaxial ellipsoid models give intermediate results (Table 7). With both contributions from the main body and rings considered, all of the models fit equally well the H_V values.

considerations used in Section 3.3.1. Table 7 summarizes the p_b and I/F using the least-squares fits to Equation (8). Figure 17 show the fits to the H_V data for the four models, which are virtually indistinguishable from each other but give substantially different relative contributions to the brightness variation in the rings and the main body. The body geometric albedo p_b does not depend strongly on the body model with values in the range 3.1%–4.2%. In contrast, the ring reflectivity I/F depends on the model adopted for the body. For instance, the spherical model attributes all of the photometric variability to the ring, resulting in $I/F = 8.9\%$, close to the previously found value for a spherical body (Braga-Ribas et al. 2014). However, the Jacobi model attributes most of the variability to the changing aspect of Chariklo, resulting in a significantly darker ring, $I/F = 0.6\%$. The Maclaurin and the generic ellipsoidal models give intermediate results with $I/F = 3.4\%$ and $I/F = 4.9\%$, respectively, but lower than previously estimated values for a non-spherical body (Braga-Ribas et al. 2014; Duffard et al. 2014).

The reflectivity I/F can be related to the albedo of the ring particles p_p in two extreme regimes: a monolayer ring where the ring thickness is comparable to the particle size and a polylayer ring where the ring thickness is large compared to the particles. Currently, there is not enough information to discriminate between these two regimes, but it is illustrative to consider them in turn here.

For a monolayer ring, the equivalent width is defined as $E_p = W(1 - f_n)$, where W is the radial width and f_n is the fractional transmission normal to the ring (Elliot et al. 1984). This gives the effective area covered by the ring particles, neglecting mutual shadowing. Taking the typical value of $E_p = 2.2$ km for the main ring C1R (Bérard et al. 2017) and the average width $W \sim 5.5$ km considered here, the geometric albedo of the ring particles is $p_p = (5.5/2.2) \times I/F$. Depending on the model used here (from sphere to Jacobi), p_p ranges from 22% to 1.5%, respectively.

In the polylayer regime, the ring reflectivity I/F can be approximated by a single scattering model (Chandrasekhar 1960),

$$I/F = \frac{p_p}{2}\left[1 - \exp\left(\frac{-2\tau_N}{\mu}\right)\right], \tag{14}$$

where $\mu = \sin(B)$ and τ_N is the ring normal optical depth. Using an approximate $\tau_N = 0.4$ measured for the main ring C1R (Braga-Ribas et al. 2014), we see that p_p is two to three times I/F, similar to the monolayer case.

The ring particles can thus be darker than those of Uranus (Karkoschka 2001), $p_p \sim 5\%$, but cannot be as bright as Saturn's ring particles (Cuzzi et al. 2009), $p_p \sim 50\%$. For the Jacobi model, the geometric albedo of the ring particles $p_p < 2\%$ is lower than those of TNOs (Lacerda et al. 2014), with geometric albedo $p \gtrsim 4\%$. This makes the Jacobi solution less plausible, giving preference to the generic ellipsoid model, which gives a geometric albedo of ring particles of $p_p = 10\%$–15%.

5.3. Comparison with Radiometric Results

Chariklo's equivalent radius[27] $r_{\rm equiv}$ was estimated from thermal measurements, with values ranging from 108 km to 151 km (Jewitt & Kalas 1998; Altenhoff et al. 2001; Sekiguchi et al. 2012; Bauer et al. 2013; Fornasier et al. 2014).

For the Maclaurin model, $r_{\rm equiv}$ only depends on the opening angle, while for the Jacobi models, it also depends on the rotation angle. Although observed values are compatible at the 2σ level with our models (with $r_{\rm equiv}$ ranging between 110 km and 140 km), they should be taken with caution because the published radius values were estimated from simplified models (using NEATM, in some cases even assuming a particular value of the beaming factor) or from more elaborate thermophysical models but without knowledge of pole orientation, and in particular, because all models assumed spherical shapes.

For the comparison to be realistic, a reanalysis of the thermal data is thus necessary to take into account the different shape models and changes in orientation with time, and to estimate the possible ring contribution to the thermal emission. These aspects are explored in Lellouch et al. (2017).

6. Conclusions

The combination of results from stellar occultations with a quantitative statistical approach is a powerful tool to derive the sizes and shapes of small and distant objects. In the case of the Centaur object Chariklo, this is of great importance for constraining the dynamics of its ring system.

In this work, we explored four models for Chariklo's main body shape: a sphere, a triaxial ellipsoid, a Maclaurin spheroid, and a Jacobi ellipsoid. Using a Bayesian approach, we combine five stellar occultations observed between 2013 and 2016 with rotation light curves to derive credible intervals for the size, shape, and density of Chariklo.

[27] Defined as $r_{\rm equiv} = \sqrt{A/\pi}$, where A is the apparent surface area of the body, not to be confused with the volumetric equivalent radius $R_{\rm equiv}$ of each model, which does not depend on orientation.

Using the spherical model, we find that topographic features with heights of about 9% of Chariklo's radius can explain our observations. This is comparable to the values of small icy bodies of similar size and density as Hyperion and Phoebe. However, we observe a clear correlation of the radial residuals with the position angle along the limb, being positive near the equator and negative near the pole. This strongly suggests that Chariklo is flattened or elongated.

The ellipsoidal and Jacobi models are consistent with the stellar occultation data, the rotational light curve amplitude, and in the case of the occultation of 2013, with the expected rotation phase. This suggests that Chariklo is an elongated body.

Clearly, an improved value of Chariklo's rotational period will constrain the rotational angle at each occultation date, and thus reduce the number of free parameters of the models.

Accounting for the fact that Chariklo may have an oblate or ellipsoidal shape, we find that the ring reflectivity is much less constrained than previously considered. Although a spherical shape for the body implies ring particles four times brighter than Uranus ring particles, the Jacobi model may result in ring particles that are twice darker. This large range of uncertainty is a strong incentive for improving our knowledge of Chariklo's size and shape, using better predicted events in the *Gaia* era, thus allowing well-sampled stellar occultations.

The density obtained in the cases of the Jacobi and Maclaurin models is in the range 800–1250 kg m^{-3}, indicative of an icy body. This must be taken with caution, though, as this assumes a homogeneous body in hydrostatic equilibrium. The corresponding mass range is 6–8 $\times$ 10^{18} kg. With that value, it is interesting to note that the 3:1 resonance between the mean motion of the particles and the rotation of the body[28] is located at the radius 408 $\pm$ 20 km, close to the radii of C1R and C2R, respectively 391 km and 405 km. The potential implications of this resonance will be considered in another work.

R.L. acknowledges support from CONICYT-PCHA/Doctorado Nacional/2014-21141198. The authors acknowledge support from the French grant "Beyond Neptune II" ANR-11-IS56-0002. Part of the research leading to these results has received funding from the European Research Council under the European Community's H2020 (2014-2020/ERC Grant Agreement n° 669416 "LUCKY STAR"). The research leading to these results has received funding from the European Union's Horizon 2020 Research and Innovation Programme, under Grant Agreement N°. 687378, project SBNAF. E.M. acknowledges support from the Contrato de subvención 205-2014 Fondecyt—Concytec, Perú. J.I.B.C. acknowledges the CNPq grant n° 308150/2016-3. M.A. thanks the CNPq (Grants 473002/2013-2 and 308721/2011-0) and FAPERJ (Grant E-26/111.488/2013). G.B.-R. acknowledges the support of the CAPES (203.173/2016) and FAPERJ/PAPDRJ (E26/200.464/2015-227833) grants. R.V.-M. thanks grants CNPq-306885/2013, Capes/Cofecub-2506/2015, Faperj: PAPDRJ-45/2013, and E-26/203.026/2015. This work is partly based on observations performed at the MPG 2.2 meter telescope, program CN2016A-87. Based on observations obtained at the SOAR telescope, program SO2015A-015. The 50 cm telescopes used for the Hakos observations belong to the IAS observatory at Hakos/Namibia. This work was partially supported by the National Research Foundation of South Africa and contains data taken at the South African Astronomical Observatory (SAAO). This work has made use of data from the European Space Agency (ESA) mission *Gaia* (https://www.cosmos.esa.int/gaia), processed by the *Gaia* Data Processing and Analysis Consortium (DPAC; https://www.cosmos.esa.int/web/gaia/dpac/consortium). Funding for DPAC has been provided by national institutions, in particular the institutions participating in the *Gaia* Multilateral Agreement.

Facilities: SOAR (SOI), Max Planck:2.2 m (WFI), LNA: BC0.6m.

Software: DanDIA (Bramich 2008), IRAF (Tody 1986), emcee (Foreman-Mackey et al. 2013).

[28] At this resonance, a ring particle undergoes one revolution while Chariklo completes three rotations.

ORCID iDs

R. Leiva https://orcid.org/0000-0002-6477-1360
B. Sicardy https://orcid.org/0000-0003-1995-0842
D. Bérard https://orcid.org/0000-0001-7654-6809
E. Lellouch https://orcid.org/0000-0001-7168-1577
E. Meza https://orcid.org/0000-0002-4058-0420
P. Kervella https://orcid.org/0000-0003-0626-1749
C. Snodgrass https://orcid.org/0000-0001-9328-2905
R. Duffard https://orcid.org/0000-0001-5963-5850
G. Benedetti-Rossi https://orcid.org/0000-0002-4106-476X
M. Assafin https://orcid.org/0000-0002-8211-0777
J.-L. Dauvergne https://orcid.org/0000-0002-4058-0420
L. Maquet https://orcid.org/0000-0002-3443-5841

References

Altenhoff, W. J., Menten, K. M., & Bertoldi, F. 2001, A&A, 366, L9
Alvarez-Candal, A., Ortiz, J. L., Morales, N., et al. 2014, A&A, 571, A48
Bauer, J. M., Grav, T., Blauvelt, E., et al. 2013, ApJ, 773, 22
Belskaya, I., Bagnulo, S., Barucci, M., et al. 2010, Icar, 210, 472
Benedetti-Rossi, G., Sicardy, B., Buie, M. W., et al. 2016, AJ, 152, 156
Bérard, D., Sicardy, B., Camargo, J. I. B., et al. 2017, AJ, 154, 144
Braga-Ribas, F., Sicardy, B., Ortiz, J. L., et al. 2014, Natur, 508, 72
Braga-Ribas, F., Sicardy, B., Ortiz, J. L. J., et al. 2013, ApJ, 773, 26
Bramich, D. M. 2008, MNRAS Letters, 386, L77
Britt, D. T., Yeomans, D., Housen, K., & Consolmagno, G. 2002, in Asteroids III, ed. W. F. J. Bottke et al. (Tucson, AZ: Univ. Arizona Press), 485
Brown, M. E. 2013, ApJ, 767, L7
Camargo, J. I. B., Vieira-Martins, R., Assafin, M., et al. 2014, A&A, 561, A37
Carry, B. 2012, P&SS, 73, 98
Castillo-Rogez, J., Matson, D., Sotin, C., et al. 2007, Icar, 190, 179
Castillo-Rogez, J. C., Johnson, T., Thomas, P., et al. 2012, Icar, 219, 86
Chandrasekhar, S. 1960, Radiative Transfer (New York: Dover), 393
Chandrasekhar, S. 1987, Ellipsoidal Figures of Equilibrium (New York: Dover), 264
Cuzzi, J., Clark, R., Filacchione, G., et al. 2009, in Saturn from Cassini-Huygens, Ring Particle Composition and Size Distribution, ed. M. Dougherty, L. Esposito, & S. Krimigis (Dordrecht: Springer Netherlands), 459
Davies, J. K., McBride, N., Ellison, S. L., Green, S. F., & Ballantyne, D. R. 1998, Icar, 134, 213
Desmars, J., Camargo, J. I. B., Braga-Ribas, F., et al. 2015, A&A, 584, A96
Dias-Oliveira, A., Sicardy, B., Ortiz, J. L., et al. 2017, AJ, 154, 22
Duffard, R., Pinilla-Alonso, N., Ortiz, J. L., et al. 2014, A&A, 568, A79
Elliot, J. L., French, R. G., Meech, K. J., & Elias, J. H. 1984, AJ, 89, 1587
Elliot, J. L., Person, M. J., Zuluaga, C. A., et al. 2010, Natur, 465, 897
Fernandez-Valenzuela, E., Ortiz, J. L., Duffard, R., Morales, N., & Santos-Sanz, P. 2017, MNRAS, 466, 4147
Foreman-Mackey, D., Hogg, D. W., Lang, D., & Goodman, J. 2013, PASP, 125, 306
Fornasier, S., Lazzaro, D., Alvarez-Candal, A., et al. 2014, A&A, 568, L11
Gaia Collaboration, Brown, A. G. A., Prusti, T., et al. 2016a, A&A, 595, A1
Gaia Collaboration, Lindegren, L., Lammers, U., et al. 2016b, A&A, 595, A2
Galiazzo, M., Marcos, C. D. L. F., Marcos, R. D. L. F., et al. 2016, Ap&SS, 361, 212

Goodman, J., & Weare, J. 2010, Communications in Applied Mathematics and Computational Science, 5, 65
Gregory, P. 2005, Bayesian Logical Data Analysis for the Physical Sciences: A Comparative Approach with Mathematica Support (1st ed.; Cambridge: Cambridge Univ. Press), 488
Guilbert-Lepoutre, A. 2011, AJ, 141, 103
Jewitt, D., & Kalas, P. 1998, ApJ, 499, L103
Karkoschka, E. 2001, Icar, 151, 51
Kervella, P., Thévenin, F., Di Folco, E., & Ségransan, D. 2004, A&A, 426, 297
Lacerda, P., Fornasier, S., Lellouch, E., et al. 2014, ApJ, 793, L2
Lellouch, E., Moreno, R., & Muller, T. 2017, A&A, in press
Ortiz, J. L., Sicardy, B., Braga-Ribas, F., et al. 2012, Natur, 491, 566
Peixinho, N., Lacerda, P., Ortiz, J. L., et al. 2001, A&A, 371, 753
Schindler, K., Wolf, J., Bardecker, J., et al. 2017, A&A, 600, A12
Sekiguchi, T., Ootsubo, T., Hasegawa, S., et al. 2012, in Asteroids, Comets, Meteors, LPI Contribution No. 1667 (Houston, TX: Lunar and Planetary Institute), 6477
Sicardy, B., Colas, F., Maquet, L., et al. 2010, BAAS, 42, 993
Sicardy, B., Ortiz, J. L., Assafin, M., et al. 2011, Natur, 478, 493
Thomas, P. C. 1989, Icar, 77, 248
Tody, D. 1986, Proc. SPIE, 627, 733
Widemann, T., Sicardy, B., Dusser, R., et al. 2009, Icar, 199, 458
Zacharias, N., Monet, D., Levine, S., et al. 2004, BAAS, 36, 1418